Cell Stem Cell

Article

# Increased cholesterol synthesis drives neurotoxicity in patient stem cell-derived model of multiple sclerosis

## Graphical abstract

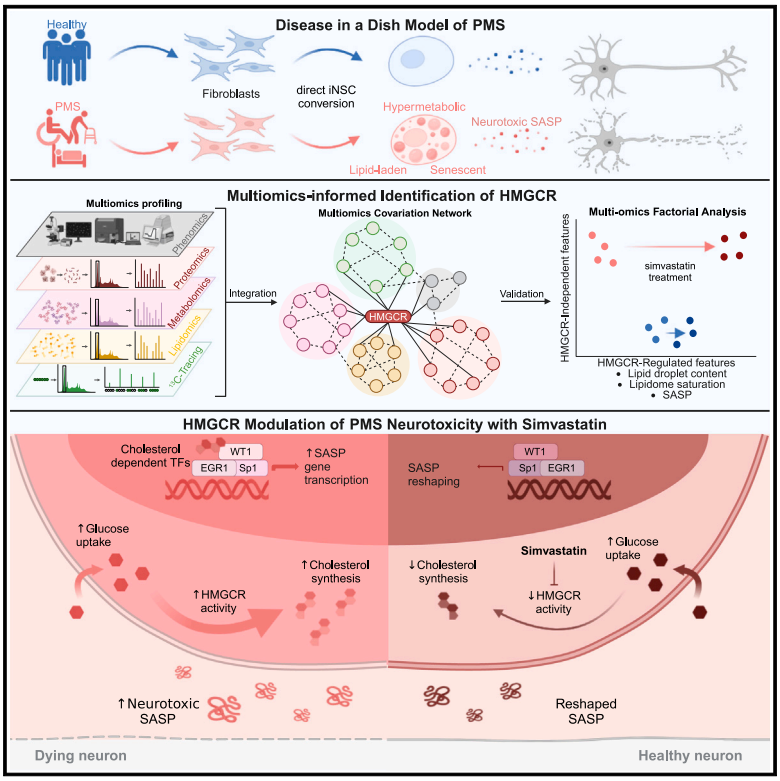


## Highlights

- PMS iNSCs are senescent, inflammatory, and hypermetabolic
- Glucose fuels cholesterol synthesis in PMS iNSCs
- HMGCR triggers lipogenesis and paracrine neurotoxicity via SASP in PMS iNSCs
- Pharmacological inhibition of HMGCR reshapes the SASP and reduces neurotoxicity


## Authors

Rosana-Bristena Ionescu, Alexandra M. Nicaise, Julie A. Reisz, ..., Irina Mohorianu, Angelo D'Alessandro, Stefano Pluchino

## Correspondence

angelo.dalessandro@cuanschutz.edu (A.D.),
spp24@cam.ac.uk (S.P.)



## In brief

Ionescu, Nicaise, and colleagues reveal that induced neural stem cells (iNSCs) from patients with progressive multiple sclerosis (PMS) are senescent and exhibit a hypermetabolic phenotype linked to increased cholesterol synthesis. Small-molecule-based inhibition of cholesterol synthesis modifies the neurotoxic secretome of PMS iNSCs, enhancing their cytoprotective properties.


Ionescu et al., 2024, Cell Stem Cell *31*, 1574–1590
November 7, 2024 
https://doi.org/10.1016/j.stem.2024.09.014

CellPress

CellPress
OPEN ACCESS

Cell Stem Cell

Article

# Increased cholesterol synthesis drives neurotoxicity in patient stem cell-derived model of multiple sclerosis

Rosana-Bristena Ionescu,[1,10] Alexandra M. Nicaise,[1,10] Julie A. Reisz,[2] Eleanor C. Williams,[3] Pranathi Prasad,[1] Cory M. Willis,[1] Madalena B.C. Simões-Abade,[1] Linda Sbarro,[1] Monika Dzieciatkowska,[2] Daniel Stephenson,[2] Marta Suarez Cubero,[4] Sandra Rizzi,[4] Liviu Pirvan,[3] Luca Peruzzotti-Jametti,[1,5] Valentina Fossati,[6] Frank Edenhofer,[4] Tommaso Leonardi,[7] Christian Frezza,[8,9] Irina Mohorianu,[3] Angelo D'Alessandro,[2,*] and Stefano Pluchino[1,11,*]

[1]Department of Clinical Neurosciences and NIHR Biomedical Research Centre, University of Cambridge, Cambridge CB2 0AH, UK
[2]Department of Biochemistry and Molecular Genetics, University of Colorado School of Medicine, Aurora, CO 80045, USA
[3]Cambridge Stem Cell Institute, Jeffrey Cheah Biomedical Centre, University of Cambridge, Cambridge CB2 0AW, UK
[4]Genomics, Stem Cell Biology and Regenerative Medicine Group, Institute of Molecular Biology & CMBI, Leopold-Franzens-University Innsbruck, Innsbruck 6020, Austria
[5]Department of Metabolism, Digestion and Reproduction, Imperial College London, London SW7 2AZ, UK
[6]The New York Stem Cell Foundation Research Institute, New York, NY 10019, USA
[7]Center for Genomic Science of IIT@SEMM, Instituto Italiano di Tecnologia (IIT), 20139 Milan, Italy
[8]Institute for Metabolomics in Ageing, Cluster of Excellence Cellular Stress Responses in Aging-associated Diseases (CECAD), University of Cologne, Faculty of Medicine and University Hospital Cologne, Cologne 50931, Germany
[9]Institute of Genetics, Faculty of Mathematics and Natural Sciences, Faculty of Medicine, University of Cologne, Cologne 50674, Germany
[10]These authors contributed equally
[11]Lead contact
*Correspondence: angelo.dalessandro@cuanschutz.edu (A.D.), spp24@cam.ac.uk (S.P.)
https://doi.org/10.1016/j.stem.2024.09.014

## SUMMARY

Senescent neural progenitor cells have been identified in brain lesions of people with progressive multiple sclerosis (PMS). However, their role in disease pathobiology and contribution to the lesion environment remains unclear. By establishing directly induced neural stem/progenitor cell (iNSC) lines from PMS patient fibroblasts, we studied their senescent phenotype *in vitro*. Senescence was strongly associated with inflammatory signaling, hypermetabolism, and the senescence-associated secretory phenotype (SASP). PMS-derived iNSCs displayed increased glucose-dependent fatty acid and cholesterol synthesis, which resulted in the accumulation of lipid droplets. A 3-hydroxy-3-methylglutaryl (HMG)-coenzyme A (CoA) reductase (HMGCR)-mediated lipogenic state was found to induce a SASP in PMS iNSCs via cholesterol-dependent transcription factors. SASP from PMS iNSC lines induced neurotoxicity in mature neurons, and treatment with the HMGCR inhibitor simvastatin altered the PMS iNSC SASP, promoting cytoprotective qualities and reducing neurotoxicity. Our findings suggest a disease-associated, cholesterol-related, hypermetabolic phenotype of PMS iNSCs that leads to neurotoxic signaling and is rescuable pharmacologically.

## INTRODUCTION

Multiple sclerosis (MS) affects 2.8 million individuals worldwide, making it the most common inflammatory autoimmune demyelinating disease of the central nervous system (CNS).[1] Progressive MS (PMS) represents the late stage of the disease marked by a steady and unrelenting accumulation of chronic neurological disability as an outcome of continuing neuronal loss.[2] In PMS, immune-dependent and -independent mechanisms of disease progression/pathology have been described over the years.[3] There is limited availability of disease-modifying therapies for people with PMS due to the complexity of the disease, which has made it particularly challenging to identify targets that promote neuroprotection.[3] Hence, the identification of key mechanisms of disease and the development of a new class of disease-modifying therapies capable of effectively promoting neuroprotection to slow disease progression are critical unmet needs for people with PMS.[3]

PMS shares many pathological hallmarks with classic neurodegenerative diseases,[4] with age being the primary risk factor for the progression of disease.[5] Longitudinal magnetic resonance imaging analysis of the brains of people with MS revealed signatures indicative of advanced brain aging compared with both healthy individuals and patients diagnosed with other neurodegenerative disorders, including dementia.[6,7]

 

CellPress
OPEN ACCESS

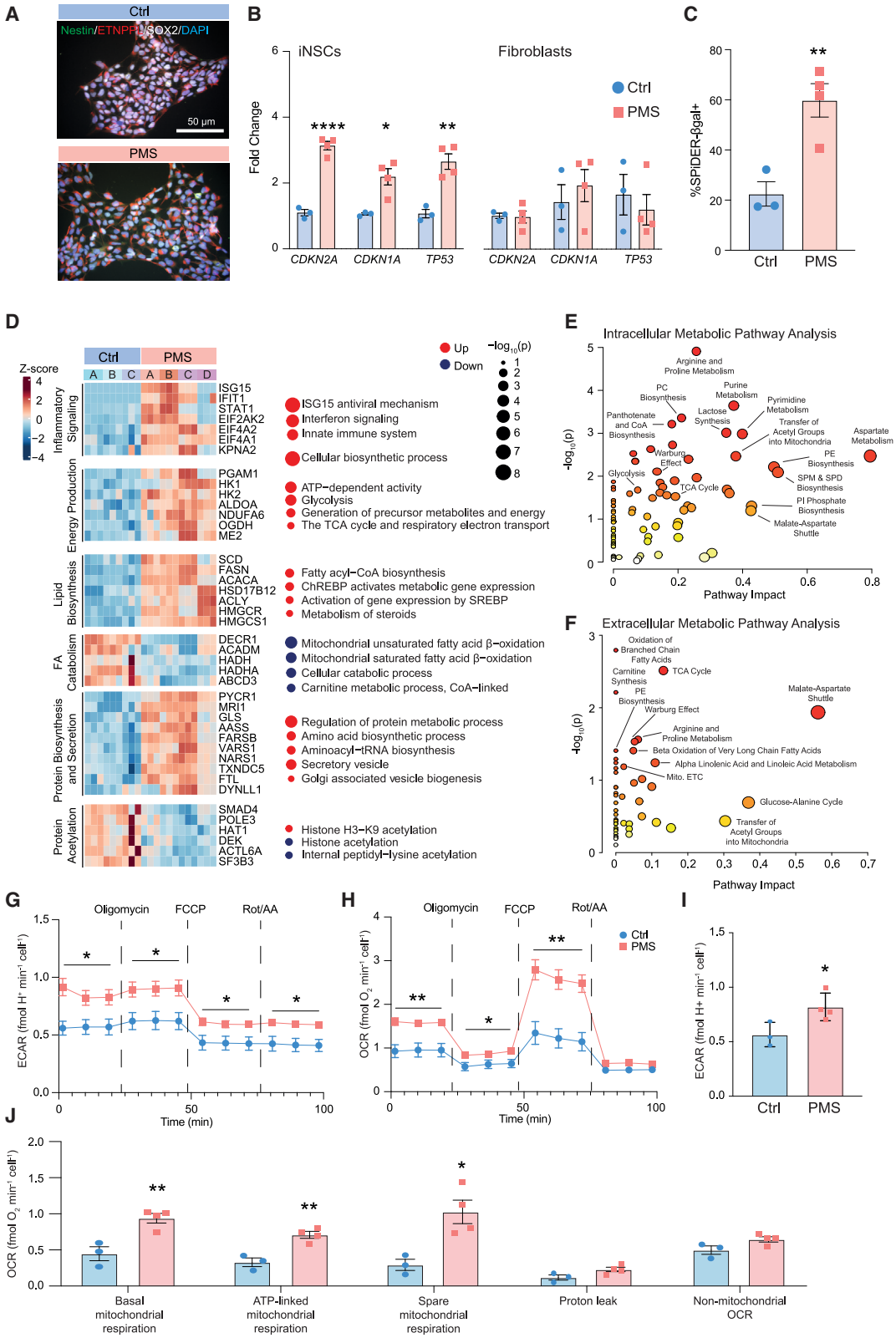


**Figure 1. PMS iNSC lines exhibit senescence-associated inflammatory signaling and hypermetabolism**

(A) Immunocytochemistry of NSC markers in Ctrl and PMS iNSC lines. Scale bar: 50 μm.

(B) mRNA expression of senescence-associated genes in iNSCs and fibroblasts.

*(legend continued on next page)*

As individuals undergo biological aging, so do their cells. Cellular aging and senescence are both characterized by gain-of-function maladaptive processes and the loss-of-homeostatic processes that disrupt normal cellular functions.[8] Multiple independent post-mortem pathological studies of human individuals at advanced age or patients with neurodegenerative diseases have shown an accumulation of senescent cells in the brain.[9,10] When cells experience injury or disease, they undergo *adaptive cellular reprogramming*,[11] leading to the expression of immature markers and the development of a new cell state that might instigate metabolic changes and senescence.[12,13] Moreover, human single-nuclear sequencing analyses of the post-mortem MS brain[14] and genome-wide association studies have identified transcriptional states and genetic variants indicative of intrinsic cell dysfunctions associated with altered cellular energetics and senescent states.[15,16] Our analysis of these datasets revealed an immature cell state within astrocyte clusters resembling radial glia (RG)-like neural stem cells (NSCs) expressing transcriptional markers of senescence, predominantly localized in chronic active lesions.[17] Histopathological analysis has also pinpointed senescent RG-like NSCs within lesions of PMS brains.[18] In this context, senescent cells could exacerbate chronic inflammation through the release of inflammatory mediators, leading to neuronal death sustaining progressive neurodegeneration. The implications of senescent, dysfunctional RG-like NSCs and their impact on the acceleration of brain aging and neuronal functionality in PMS are yet to be established.

Cellular metabolism is a key component of senescence and disease-associated mechanisms. Hypermetabolism has been described in erythrocytes,[19] fibroblasts,[20] and astrocytes[21] from people with MS and in the context of physiological aging.[22] Analysis of cerebrospinal fluid from individuals with MS revealed dysregulated metabolic features in glucose and energy pathways, amino acid metabolism, and lipid formation and breakdown.[23] Lipid metabolism is involved in controlling NSC homeostasis and is linked as a major regulator of cellular senescence and the SASP.[24,25] Whether an altered metabolic state is present in senescent NSCs from individuals with PMS is unknown.

Reprogramming technologies that revert somatic cells to an embryonic-like state (induced pluripotent stem cells [iPSCs]) or directly convert to cell types are being extensively applied to establish disease-in-a-dish human models of CNS disorders that cannot be fully recapitulated using animal models.[26,27] iPSC-derived CNS cells have been effectively used to model intrinsic cellular dysfunctions of MS. By studying these systems, abnormalities have been found in mitochondrial function, junction integrity, and the development of a (resting) inflammatory state.[21,28–31] Senescent features have been described in iPSC-NSCs derived from people with PMS, including a SASP that was found to inhibit oligodendrocyte progenitor cell differentiation.[18]

In our efforts to model RG-like NSCs, we generated iNSCs directly from individuals with PMS and unaffected controls, aiming for increased fidelity in preserving the aging characteristics of the donors.[17,32] Our investigations revealed lipid droplet (LD) accumulation as a central pathological feature in PMS iNSCs that originated from glucose-derived, 3-hydroxy-3-methylglutaryl-coenzyme A (CoA) reductase (HMGCR) activity-dependent cholesterol synthesis. We identified that heightened HMGCR activity in PMS iNSCs governs the neurotoxic SASP, which can be reshaped with the HMGCR inhibitor simvastatin.

Our findings shed light on how a hypermetabolic state supporting cholesterol biosynthesis transcriptionally governs the neurotoxic SASP in PMS iNSCs. This underscores the potential involvement of NSC metabolism in the progression of disability and neurodegeneration observed in the PMS brain.

## RESULTS

### PMS iNSCs show senescent gene expression linked to inflammation and hypermetabolism

We first confirmed previous findings of senescence in PMS NSCs[18] by generating iPSCs from skin-derived fibroblasts (Figures S1A and S1B; Table S1). We derived endodermal, mesodermal, and ectodermal iPSC progenies (Figure S1C) and found significantly increased expression of the cellular senescence marker *CDKN2A* in only the PMS ectodermal progenies (Figure S1D). The acquisition of an ectodermal NSC identity in PMS cells is associated with increased expression of senescence-associated genes in a cell-autonomous fashion.

As iPSC reprogramming has been demonstrated to rejuvenate the epigenome,[33] we next utilized direct reprogramming technology to generate cell lines that retain aging-related markers.[17] We reprogrammed skin fibroblasts from 3 non-diseased individuals (Ctrl) and 4 people with PMS between 25 and 63 years of age into iNSCs (Table S1).[32,34] Quality control analysis by immunocytochemistry showed superimposable expression of established RG-like/NSC markers NESTIN, SOX2, and ETNPPL in both Ctrl and PMS iNSC lines (Figure 1A).[17] Reverse transcription polymerase chain reaction (RT-PCR) of *NESTIN*, *SOX2*, and *PAX6* confirmed comparable expression levels across all iNSC lines and the absence of the pluripotency marker gene *OCT4* and Sendai virus vectors (Figure S1E; Table S2).

(C) Expression of SPiDER-βgal in iNSC lines (as in Figures S1F and S1G).
(D) Pathway enrichment analysis of gene onotlogy (GO) and reactome (REACT) terms in PMS vs. Ctrl iNSC lines based on intracellular proteomics. Differentially enriched proteins and pathways were considered significant at adjusted $p \leq 0.05$ (Benjamini-Hochberg correction) under edgeR and hypergeometric tests, respectively.
(E and F) Metabolic pathway analysis of intracellular (E) and extracellular (F) metabolites. Differentially abundant metabolites were considered significant at adjusted $p \leq 0.05$ (Benjamini-Hochberg correction) under Wilcox rank sum.
(G and H) ECAR (G) and OCR (H) over time during a mitochondrial stress test in the presence of glucose, pyruvate, and glutamine.
(I) Basal ECAR quantified as in (G).
(J) Quantification of basal mitochondrial respiration, ATP-linked mitochondrial respiration, spare mitochondrial respiration, mitochondrial respiration linked to proton leak, and non-mitochondrial OCR using the mitochondrial stress test.
Experiments in (B)–(J) were done on $n = 3$ Ctrl and $n = 4$ PMS iNSC lines, each performed in $n \geq 3$ replicates. Data in (B), (C), and (G)–(J) are as mean values ± SEM. $^{*}p \leq 0.05$, $^{**}p \leq 0.01$, $^{****}p \leq 0.0001$. unpaired t test.

The expression of *CDKN2A*, *CDKN1A*, and *TP53* was significantly increased in PMS iNSC lines (vs. Ctrl iNSC lines) (Figure 1B),[17] whereas no differences were identified when comparing the parental PMS and Ctrl fibroblasts (Figure 1B). We also found increased senescence-associated β-galactosidase (β-gal) expression in PMS iNSC lines using the SPiDER-βgal probe (59.8 ± 13% vs. 22.5 ± 8.4% in Ctrl iNSC lines) (Figures 1C, S1F, and S1G).

We next performed mass spectrometry-based untargeted intracellular proteomics to uncover senescence-associated dysfunctional pathways. Principal-component analysis (PCA) underlined separation between groups, with an outlier in the Ctrl line C second technical replicate (Figure S1H), though this sample had a similar proteomic makeup (in terms of expression patterns) as the other Ctrl cell lines (Figure 1D). Protein set enrichment analysis of up- and downregulated proteins in PMS iNSC lines (vs. Ctrl iNSC lines) revealed biological process terms falling within two categories: (1) inflammatory signaling and (2) metabolic processes related to energy production and anabolic/catabolic balance (Figure 1D; Table S3). Upregulated proteins associated with inflammatory pathways were primarily mapped to interferon (IFN) signaling (interferon-stimulated gene 15 [ISG15] and signal transducer and activator of transcription 1 [STAT1]). Concordantly, western blot analysis confirmed significantly increased expression of ISG15, STAT1, and its active form phosphorylated (p)-STAT1 (Y701) in PMS iNSCs (Figure S1I; Table S3). Upregulated proteins linked to cell metabolism in PMS iNSC lines were found to be involved in energy production (hexokinase 2 [HK2] and NAD-dependent malic enzyme 2 [ME2]), lipid biosynthesis (stearoyl-CoA desaturase [SCD] and fatty acid synthase [FASN]), and protein biosynthesis and secretion (methylthioribose-1-phosphate isomerase 1 [MRI1] and glutaminase [GLS]) (Figure 1D). Downregulated proteins were associated with fatty acid (FA) catabolism and protein acetylation (Figure 1D). Proteomic analysis highlighted specific inflammatory and metabolic biological processes in PMS iNSC lines linked to cellular senescence.[35–37]

As changes in protein expression are not necessarily predictive of differences in cellular metabolism, we next sought evidence of metabolic rewiring in the PMS iNSCs via mass spectrometry-based analysis of the intra- and extracellular metabolome. PCA confirmed a separation of both the intra- and extracellular metabolomes of Ctrl and PMS iNSC lines (Figures S2A and S2B; Table S4). We identified several enriched metabolic pathways (Figures 1E and 1F). In the intracellular metabolome, these included energy production through glycolysis and mitochondrial respiration (e.g., tricarboxylic acid [TCA] cycle), lipid biosynthesis (e.g., transfer of acetyl groups into mitochondria), and amino acid metabolism (e.g., arginine and proline) (Figure 1E; Table S4). The energy production pathway was also reflected in the extracellular metabolome (e.g., TCA cycle and mitochondrial electron transport chain [ETC]) (Figure 1F). These findings identify a hypermetabolic rewiring in PMS iNSC lines that parallels the metabolic landscape typical of senescent cells.[25]

We functionally validated our findings by assessing cellular bioenergetics using the Seahorse mitochondrial stress test. We found that PMS iNSC lines have a significantly altered bioenergetic profile vs. Ctrl iNSC lines (Figures 1G and 1H), absent in the parental fibroblast lines (Figures S2C–S2E). This altered bioenergetic profile was reflected in the increased basal extracellular acidification rate (ECAR), basal mitochondrial respiration, ATP-linked mitochondrial respiration, and spare mitochondrial respiratory capacity in PMS vs. Ctrl iNSC lines (Figures 1I and 1J). The comparable oxygen consumption rate (OCR)/ECAR ratio between the PMS and Ctrl iNSCs suggests that increased glycolysis is directly coupled to increased oxidative phosphorylation in PMS iNSC lines (Figure S2F).

Next, we profiled cellular mechanisms underpinning the bioenergetic abnormalities of PMS iNSC lines. We first confirmed that the hypermetabolic state of PMS iNSC lines was not the result of a difference in cell size (Figure S2G). We next analyzed the mitochondrial phenotypes of the cells as potential drivers of senescence-associated hypermetabolism. We found no significant differences in mitochondrial content (Figures S2H and S2I), mitochondrial copy number (Figure S2J), and mitochondrial mass (Figure S2K). Similarly, there were no differences in the mitochondrial network morphology (Figures S2H and S2L–S2N), membrane potential (Figure S2O), and superoxide production (Figure S2P). These data suggest that intrinsic mitochondrial changes, measured using confocal resolution, were not responsible for the observed hypermetabolic state of PMS iNSCs, which instead is linked with senescence-associated expression signatures related to inflammatory signaling and functional metabolic rewiring.

## Glucose fuels increased synthesis of lipid precursors in PMS iNSCs

We next looked at the potential extrinsic drivers of the hypermetabolic state in PMS iNSC lines, focusing on differences in mitochondrial substrate utilization. Ctrl and PMS iNSC lines cultured for 24 h in basal media actively consumed glucose and pyruvate, coupled with the production of glutamine (Figure 2A). However, extracellular glucose levels were significantly decreased and extracellular lactate was significantly higher in PMS iNSCs, while glutamine and pyruvate levels were comparable between groups (Figure 2A).

This observed metabolic phenotype in the PMS iNSCs may be the result of increased glucose utilization. To test this, we employed serial stable isotope tracing experiments with [$^{13}C_6$] glucose to determine its intracellular fate (Figure 2B). At 30 min, we found that glycolysis was more active in PMS iNSC lines (vs. Ctrl iNSC lines), as suggested by significant $^{13}C_3$ enrichment of all mid and late glycolytic metabolites (from glyceraldehyde 3-phosphate through pyruvate and lactate) (Figure 2C). Significantly increased levels of $^{13}C_6$ 6-phosphogluconate and $^{13}C_5$ ribose phosphate were also observed in the PMS iNSC lines, indicating higher glucose utilization through the pentose phosphate pathway (PPP) (Figure 2C). At 24 h, PMS iNSC lines also showed an enrichment of $^{13}C$-labeled isotopologs of TCA intermediates (citrate, aconitate, α-ketoglutarate, succinate, fumarate, and malate), indicative of increased usage of glucose-derived carbons in the TCA cycle (Figures 2D and S3A). However, the proportion of [$^{13}C_6$]glucose-labeled TCA intermediates was found to decrease as the cycle progressed beyond α-ketoglutarate, implying an alternate carbon source for the lower segments of the TCA cycle (Figure S3A).

To assess whether glutamine fueled the lower segment of the TCA cycle, we performed [$^{13}C_5$]glutamine tracing at 24 h.

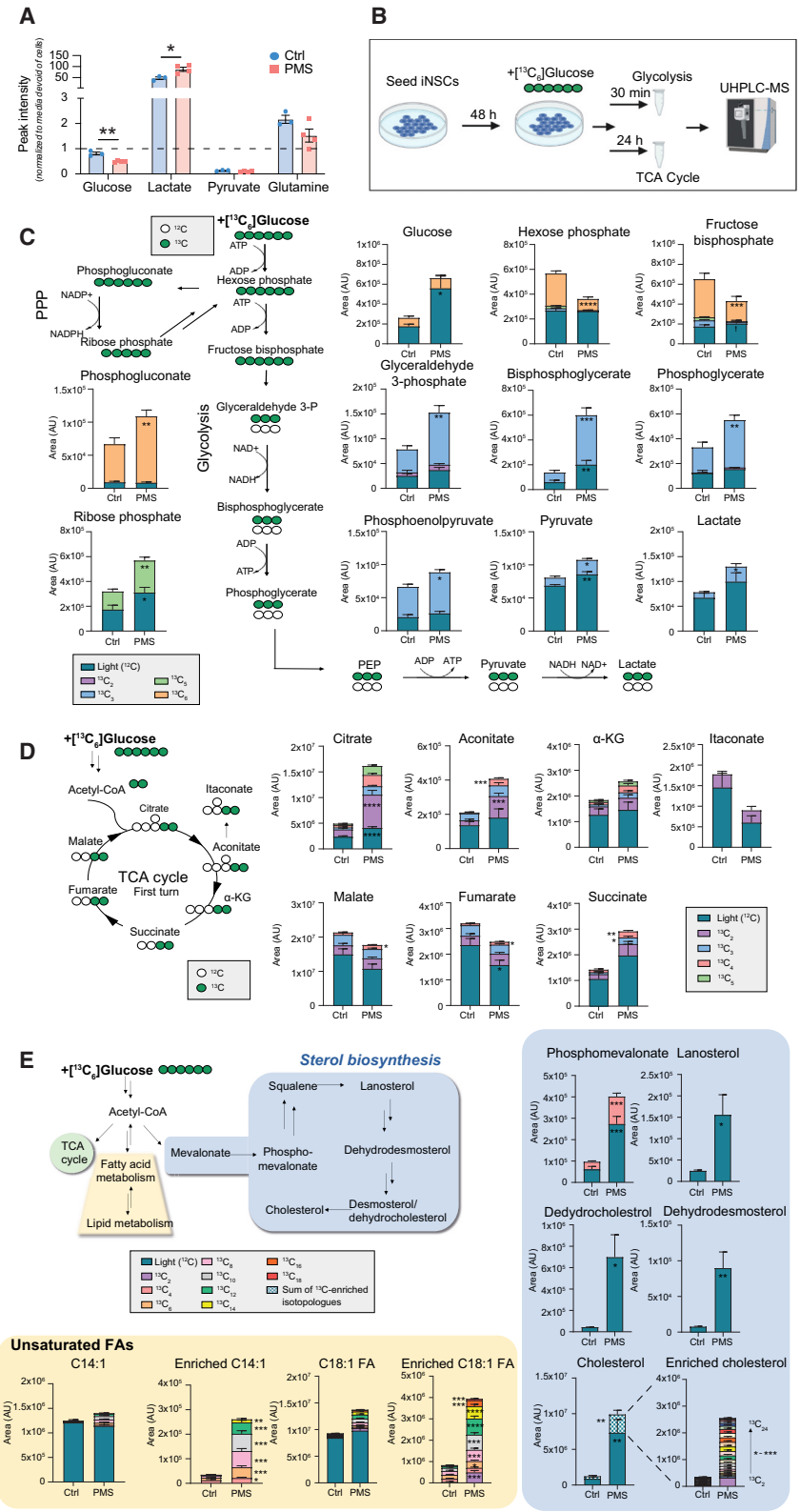


**Figure 2. PMS iNSC lines utilize glucose to support increased synthesis of lipid precursors**

(A) Relative concentrations of glucose, lactate, pyruvate, and glutamine detected by ultra high performance liquid chromatography-mass spectrometry (UHPLC-MS) in conditioned media. Values plotted over unconditioned media represented by a dashed line.

(B) Experimental schematic for [$^{13}C_6$]glucose tracing to assess glycolysis and tricarboxylic acid (TCA) cycle.

(C) Intracellular enrichment in glycolysis at 30 min following [$^{13}C_6$]glucose tracing as in (B). PPP, pentose phosphate pathway.

(D) Intracellular enrichment in TCA cycle at 24 h following [$^{13}C_6$]glucose tracing as in (B).

(E) Intracellular enrichment in lipid biosynthesis pathways at 24 h following [$^{13}C_6$]glucose tracing as in (B).

Experiments were done on $n = 3$ Ctrl and $n = 4$ PMS iNSC lines, each performed in $n \geq 3$ replicates. Data in (A) and (C)–(E) are mean values ± SEM. Stable isotope tracing data (C–E) are presented as peak areas (arbitrary units). $^{*}p \leq 0.05$, $^{**}p \leq 0.01$, $^{***}p \leq 0.001$, $^{****}p \leq 0.0001$, unpaired t test.

CellPress
OPEN ACCESS

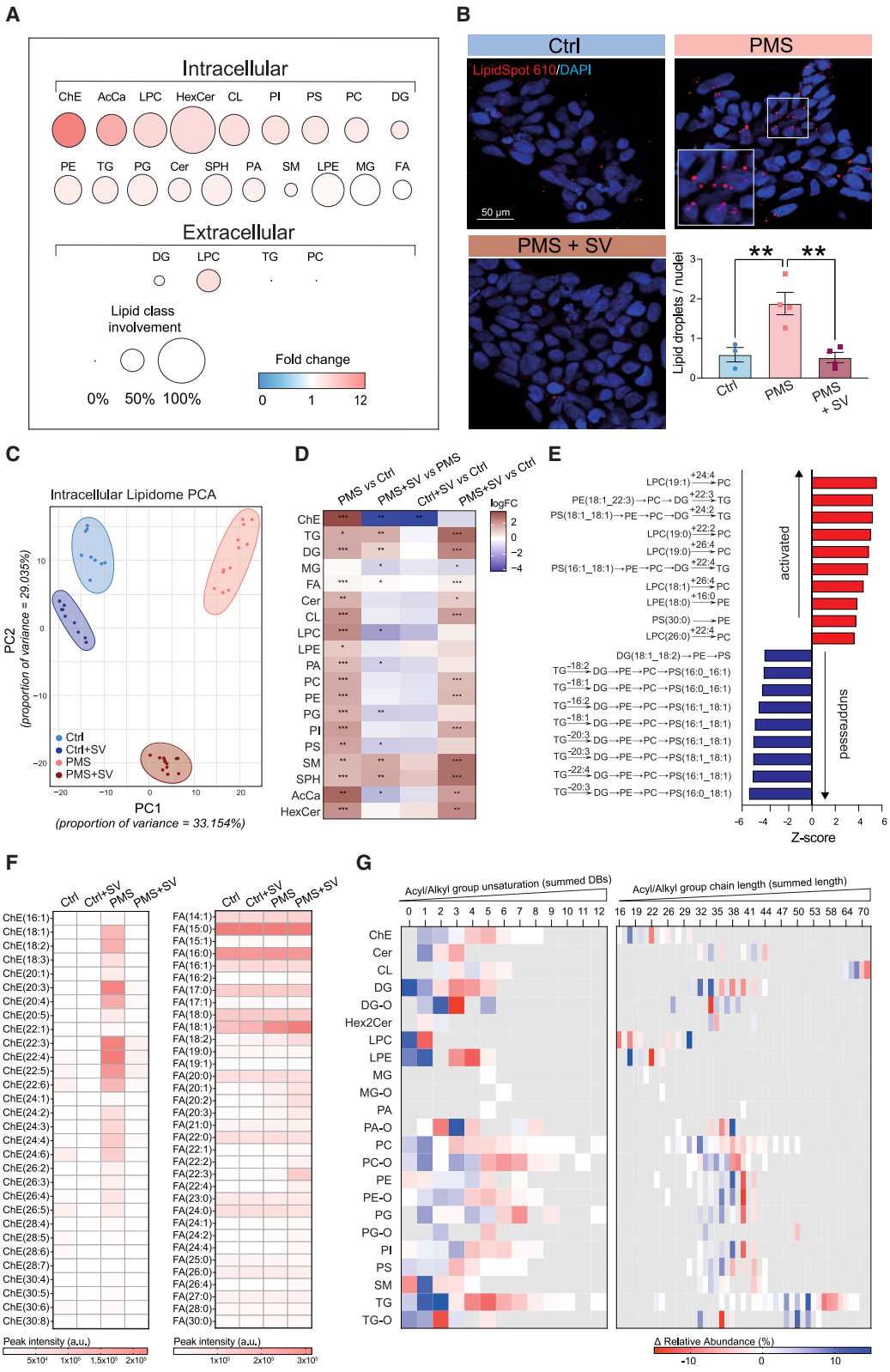


**Figure 3. HMGCR pharmacological inhibition restructures the lipidome of PMS iNSC lines**

(A) Abundance and involvement of lipid classes in PMS vs. Ctrl iNSC lines. Represented by fold change (FC) and proportion of differentially abundant lipid species within each lipid class.

*(legend continued on next page)*

Consistent with the labeled glucose tracing experiments, we observed elevated total levels of TCA cycle metabolites in PMS iNSC lines and an increased proportion of [$^{13}C_5$]glutamine-labeled TCA intermediates in the lower half of the TCA cycle (Figure S3B). These results suggest that in PMS iNSC lines, a fraction of the glucose-derived citrate exits the mitochondria into the cytosol, whereas the glutamine-derived carbons preferentially supply the lower segments of the TCA cycle.

We next focused on understanding the fate of the increased pool of glucose-derived citrate that exited the mitochondria. We explored two possible pathways related to cytoplasmic citrate on the basis of the proteomics findings: (1) protein acetylation and (2) lipid biosynthesis.[38] We compared global protein acetylation levels following [$^{13}C_6$]glucose tracing between groups and found no differentially acetylated proteins (Figure S3C). By contrast, [$^{13}C_6$]glucose tracing at 24 h revealed an increase in the concentration of $^{13}C$ labeled lipid precursors (Figures 2E and S3D). We found that $^{13}C$ enrichment in all FAs (from C10 through C18) was higher in PMS iNSC lines, particularly in unsaturated FAs (Figures 2E and S3D), compared with their saturated counterparts (Figure S3E). This suggests that the increased accumulation of unsaturated FAs in PMS iNSC lines is caused by an increase in *de novo* FA synthesis from glucose and FA desaturation.

Interrogation of the cholesterol biosynthesis pathway, both total and $^{13}C$-enriched levels, showed an increased activation in all PMS iNSC lines. Total cholesterol and levels of $^{13}C$-enriched cholesterol and isotopologs were significantly elevated in PMS iNSC lines (Figure 2E). The metabolic rewiring of PMS iNSC lines is linked with altered glucose and glutamine metabolism that ultimately leads to the increased biosynthesis of lipid precursors such as cholesterol and unsaturated FAs.

## Cholesterol synthesis leads to the accumulation of LDs and lipidome saturation

To investigate the fate of increased lipid precursor production in PMS iNSC lines, we subjected cell pellets and their conditioned media (CMs) to an untargeted mass spectrometry-based lipidomic analysis. We found that PMS iNSC lines harbor a distinct intracellular lipid signature, with multiple lipid classes being increased (vs. Ctrl iNSC lines; Figure 3A; Table S4). The lipid class that exhibited the biggest induction within the PMS iNSC lines was cholesteryl esters (ChEs) with 70% lipid class involvement and a 12-fold change (Figure 3A). A compositional analysis across intracellular lipid classes identified a higher proportion of shorter and more saturated acyl/alkyl groups in PMS iNSC lines (Figure S4A). Extracellularly, we found only minor differences between groups and undetectable ChE levels (Figures 3A and S4B). These data suggest that the increase in lipid precursors is accompanied by higher storage in the form of ChEs in PMS iNSC lines. Accordingly, we found significantly increased LD accumulation, with perinuclear localization, in PMS iNSC lines (Figures 3B and S4C). Overall, our results suggest that PMS iNSC lines develop a lipogenic state due to ChE accumulation associated with compositional changes in the lipidome.

Given the accumulation of ChEs and increased expression of HMGCR, we set out to test whether this pathway can be targeted to reduce the accumulation of lipids in PMS iNSC lines. We chose to use the US Food and Drug Administration (FDA)-approved oral medication simvastatin (SV) to pharmacologically inhibit HMGCR activity. Treatment of PMS iNSC lines for 48 h with SV (PMS + SV) was sufficient to reduce the LD content of PMS + SV iNSCs to Ctrl levels (Figures 3B, S4C, and S4D). We also disrupted the synthesis of triglycerides (TGs), which, together with ChEs represent the main neutral lipids in LDs. To this end, we blocked TG synthesis with a diacylglycerol O-acyltransferase 1 (DGAT1) inhibitor (A-922500) and a DGAT2 inhibitor (PF-06424439) for 48 h, which reduced LD accumulation in PMS iNSC lines (Figures S4E and S4F). These results suggest that ChEs and TGs are responsible for inducing LD accumulation in PMS iNSC lines.

We reported an increased expression of proteins FASN and SCD1. We therefore examined whether these pathways contributed to the increased LD accumulation in PMS iNSC lines. Interestingly, inhibiting FASN, using C75, had no effect on LDs, while SCD1 inhibition, using YTX-465, prevented LD accumulation in PMS iNSC lines (Figures S4E and S4F). Taken together, these results suggest that cholesterol synthesis and FA desaturation are essential for the increased LD buildup in PMS iNSCs, while FA synthesis is dispensable.

The liver X receptor (LXR) pathway is a central regulator of cholesterol transport and metabolism, lipogenesis, and LD formation, also regulating the induction of SCD1.[39–41] We next hypothesized that the observed increase in cholesterol may be responsible for the increase in FA desaturation via LXR activation. We found increased expression of the LXR target genes *ABCA1* and *APOE* in PMS iNSC lines (Figures S4G and S4H). This is further supported by the reduction of *ABCA1* expression in PMS iNSC lines by treatment with the LXR inhibitor, GSK2003, and inhibition of HMGCR with SV treatment (Figure S4G). None of the drug treatments targeting FASN, SCD1, or DGAT1 and DGAT2 altered *ABCA1* expression in PMS iNSC lines (Figure S4G). Conversely, increased *APOE* expression was unaffected by these treatments, including LXR inhibition, suggesting that *APOE* expression is independent of LXR activation (Figure S4H). Lastly, inhibiting LXR showed a slight reduction in LDs in PMS iNSC lines, not reaching statistical significance (Figures S4E and S4F). Overall, suggesting that LXR activation

(B) Analysis of LD content. The bar graph shows epifluorescence-based quantification of LDs. Scale bar: 50 μm.
(C) PCA of the intracellular lipidome.
(D) Log FC in intracellular concentrations of lipid classes as in (C).
(E) BioPAN analysis of the top activated and suppressed intracellular lipid species reactions induced by SV treatment in PMS iNSC lines.
(F) Changes in intracellular concentrations of ChE and FA species as in (C). Presented as peak areas (arbitrary units).
(G) Structural changes in lipid species as in (E). Relative abundance is expressed as percent change in acyl/alkyl group unsaturation (as summed double bonds [DBs]) and in acyl/alkyl group chain length (as summed length).
Experiments were done on $n = 3$ Ctrl and $n = 4$ PMS iNSC lines, each performed in $n \geq 3$ replicates. Data in (B) are mean values ± SEM, $^{**}p \leq 0.01$, one-way ANOVA, Tukey's multiple comparisons. Data in (D), $^{*}p \leq 0.05$, $^{**}p \leq 0.01$, $^{***}p \leq 0.001$; rank-sum.

is involved in PMS iNSC lipid metabolism and is regulated by cholesterol but does not fully account for increased LD accumulation.

Reducing LD accumulation in PMS iNSC lines via SV treatment induced a unique signature in the intracellular lipidome, while SV treatment of Ctrl iNSC lines (Ctrl + SV) induced minor lipidome changes (Figure 3C). ChEs were reduced to Ctrl levels in PMS + SV iNSC lines, while TG levels increased compared with baseline PMS iNSC lines (Figure 3D).

We then wanted to explore whether the compositional differences identified in the lipidome of PMS iNSC lines, which extended beyond changes in ChEs, can be further explained by the disruption of pre-existing lipid class reactions. Hierarchical clustering of all detectable lipid species suggested that SV treatment of PMS iNSC lines resulted in the emergence of subsets of lipid species following four types of responses (Figure S4I). Type 1 includes lipids that are different between groups (PMS vs. Ctrl) but are not affected by SV treatment. Type 2 includes lipids whose levels in PMS + SV iNSC lines were restored to values observed in Ctrl iNSC lines. Type 3 includes lipids that were found to be increased in PMS + SV iNSC lines only (vs. all groups), while type 4 includes lipids that were not affected by either the disease state (PMS vs. Ctrl) or treatment group (with or without SV). Several lipid classes had species representation across all four response types (e.g., TG, phosphatidylserine [PS], and phosphatidylcholine [PC]). To understand why lipid species behaved differently in response to SV treatment, we performed a deconvolution of lipid substructure using Linex[42] software. This analysis revealed a propensity of lipid species with higher summed acyl chain lengths and lower saturation to follow a type 1 or type 3 response (Figure S4J). Conversely, lipid species with lower summed acyl chain lengths tended to follow a type 2 or type 4 response (Figure S4J). These results suggest that the structural composition of lipids influences their response to HMGCR inhibition.

To further elucidate the mechanisms underpinning the differential responses of lipid species to SV treatment based on their structural composition, we performed network analysis at lipid class and species level using BioPAN.[43] We observed an activation of acylation reactions and a concomitant suppression of diacylation reactions involving non-ChE lipid classes (Figure S4K), which is consistent with a redistribution of acyl- groups from ChEs in LDs to other lipid classes. Specifically, the utilization of acyl groups 24:4, 22:3, 24:2, 22:2, 26:4, 16:0, and 22:4 for acylation reactions was increased, while the loss of acyl groups 18:2, 18:1, 16:2, 18:1, 20:3, 20:3, 22:4, and 20:3 in deacylation reactions was suppressed in PMS + SV iNSC lines (Figure 3E). We found that the identical acyl groups were highly engaged in the process of cholesterol esterification in PMS iNSC lines, whereas only slight increases were observed in the related FA species (Figure 3F). This suggests the presence of a dichotomic utilization of these FA species for either cholesterol esterification or acylation reactions by other lipid species in PMS iNSC lines. Accordingly, HMGCR inhibition with SV adjusted the lipid compositional profile of PMS iNSC lines by increasing the proportion of longer and less saturated acyl/alkyl groups (Figure 3G).

The diversion of the PMS iNSC metabolome toward increased LD formation by ChE synthesis leads to an altered structural and compositional landscape of the intracellular lipidome toward increased saturation and shortened acyl chain moieties.

## Cholesterol-regulated TFs induce SASP in PMS iNSCs

Lipid-laden senescent cells have been reported to exhibit a SASP.[25] To further investigate the functional implications of the "lipid laden" phenotype of PMS iNSC lines, we analyzed their secretome in CMs via untargeted mass spectrometry-based proteomics. We identified an increase in SASP factors[44–46] (e.g., tissue inhibitor of metalloproteinases 1 [TIMP1], fibronectin 1 [FN1], and matrix metalloproteinase 2 [MMP2]) in the CMs of PMS iNSC lines (Figure 4A; Table S5). We performed a protein set enrichment analysis of the up- and downregulated differentially secreted proteins (DSPs) found in the CMs. Enrichment analysis of the upregulated DSPs in the CMs from PMS iNSC lines (vs. Ctrl iNSC lines) identified biological processes associated with five categories: (1) neurite dynamics, (2) metabolic processes, (3) regulation of insulin growth factor (IGF) signaling, (4) inflammatory signaling, and (5) degradation of the extracellular matrix (ECM) (Figure 4B; Table S5). Enrichment analysis of PMS downregulated DSPs, instead, pertained to cytoprotective mechanisms such as reactive oxygen species (ROS) detoxification and modulation of apoptosis (Figure 4B).

To establish a functional correlative line of evidence on a regulatory mechanism between the lipogenic state of PMS iNSC lines and their secretory phenotype, we performed an integrative analysis of the multiple-omics datasets. This included intra- and extracellular metabolomics, intracellular proteomics, secretomics, and lipidomics. Based on this analysis, we focused on two main biological processes, denoted as parental hubs, which were overrepresented across several of the -omics datasets: LD biosynthesis and the secretory phenotype. Focusing on the top 1,000 connections (edges) between proteins, metabolites, and lipids, we found 57.5% pairs of connected entities were entirely contained within one hub. This included 40.2% (335 connections) within the secretory hub and 17.3% (153 connections) in the LD synthesis hub (Figure 4C). This revealed dense connectivity between the LD synthesis hub and the secretory hub, suggesting functionally relevant regulatory links between the lipogenic state of PMS iNSCs and their paracrine signaling.

As the secretome is transcriptionally controlled,[45,47,48] we then performed a transcription factor (TF) enrichment analysis on differentially expressed mRNA species,[17] intracellular proteins, and secreted factors. We identified six significantly enriched TF candidates (E2F1, EGR1, WT1, SP1, c-JUN, and JUNB) across all three profiled expression modalities, which could account for the expression signatures observed in the PMS iNSC lines (Figure 4D). Together, these TFs have strongly associated binding sites, trans modulatory functions, and cooperatively engage in gene regulatory networks.[49–51] The activity of several of the top identified TFs—which could account for the PMS iNSC secretome—is regulated by cholesterol (WT1,[52] c-JUN,[53] JUNB,[53] and SP1[54]), or by the metabolic pathways of cholesterol synthesis (E2F1[55]), cholesterol esterification (E2F1[56]), or FA saturation (E2F1[57]). Hence, we propose that the lipogenic state and the secretory phenotype of PMS iNSC lines are transcriptionally co-regulated.

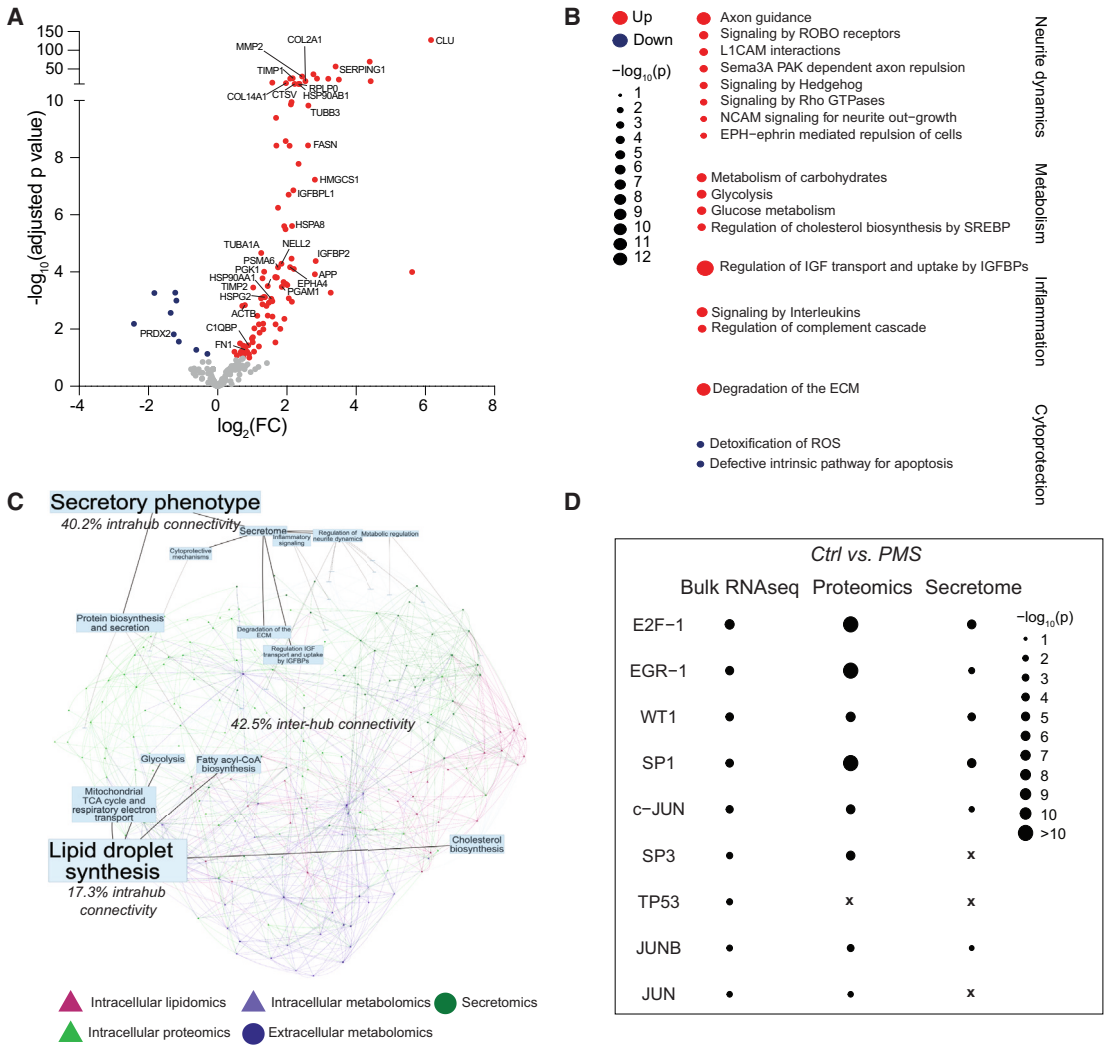


**Figure 4. PMS iNSC lines express SASP associated with cholesterol-regulated TFs**

(A) Volcano plot of DSPs in CMs from PMS and Ctrl iNSC lines. $\log_2$(FC) and $-\log_{10}$ adjusted p values are reported for each protein.

(B) Pathway enrichment analysis of biological processes (GO and REACT terms) based on DSPs in CMs from PMS and Ctrl iNSC lines. Differentially enriched biological processes were considered significant at adjusted $p \leq 0.05$ under the hypergeometric test.

(C) Covariation network PMS vs. Ctrl lines. Nodes are color-coded: proteins are represented in green, lipids in pink, metabolites in purple, with triangular nodes for intracellular and circles for extracellular metabolites or proteins. The strength of the edge between the nodes (proteins, metabolites, or lipids) represents the strength in the covariation.

(D) TF enrichment analysis of terms abased on differentially expressed genes (DEGs) by bulk RNA-sequencing (RNA-seq), proteins (DEPs) by intracellular proteomics, and DSPs as in (A). DEGs were considered significant at adjusted $p$ value $\leq 0.05$ (Benjamini-Hochberg correction) under the DESeq2 test. DEPs were considered significant at adjusted $p$ value $< 0.05$ (Benjamini-Hochberg correction) under the edgeR test. TF term enrichment was considered significant at adjusted $p \leq 0.05$ under the hypergeometric test. X is for TF terms not being differentially enriched.

Secretomics experiments were done on $n = 3$ Ctrl and $n = 4$ PMS iNSC lines, each performed in $n \geq 3$ replicates. Bulk RNA-seq data analyzed were performed on $n = 2$ Ctrl and $n = 2$ PMS iNSC lines, each performed in $n \geq 2$ replicates. DSPs in (A)–(D) were considered significant at adjusted $p$ value $< 0.1$ (Benjamini-Hochberg correction) and $|\log_2 FC| > 0.2$ under the edgeR test.

## Pharmacological inhibition of HMGCR rescues the neurotoxic secretome of PMS iNSCs

We next utilized our proteomics approach to investigate the potential regulatory role of cholesterol on the secretome by profiling the CMs of Ctrl + SV and PMS + SV iNSC lines. Our results revealed a higher number of DSPs in the CMs of PMS + SV vs. PMS iNSC lines compared with Ctrl + SV vs. Ctrl iNSC lines (Figure 5A; Table S5).

PMS + SV led to changes in levels of previously identified DSPs in the PMS iNSC secretome (ephrin type-A receptor 4 [EPHA4], TIMP2, and peroxiredoxin 2 [PRDX2]) and triggered the production of new DSPs (Figure S5A). Some of these newly induced DSPs were unique, while others were shared with the CMs of Ctrl + SV (Figure 5A). Further analysis of the identified DSPs through protein set enrichment analysis indicated that treatment with SV partially corrected the PMS iNSC secretome

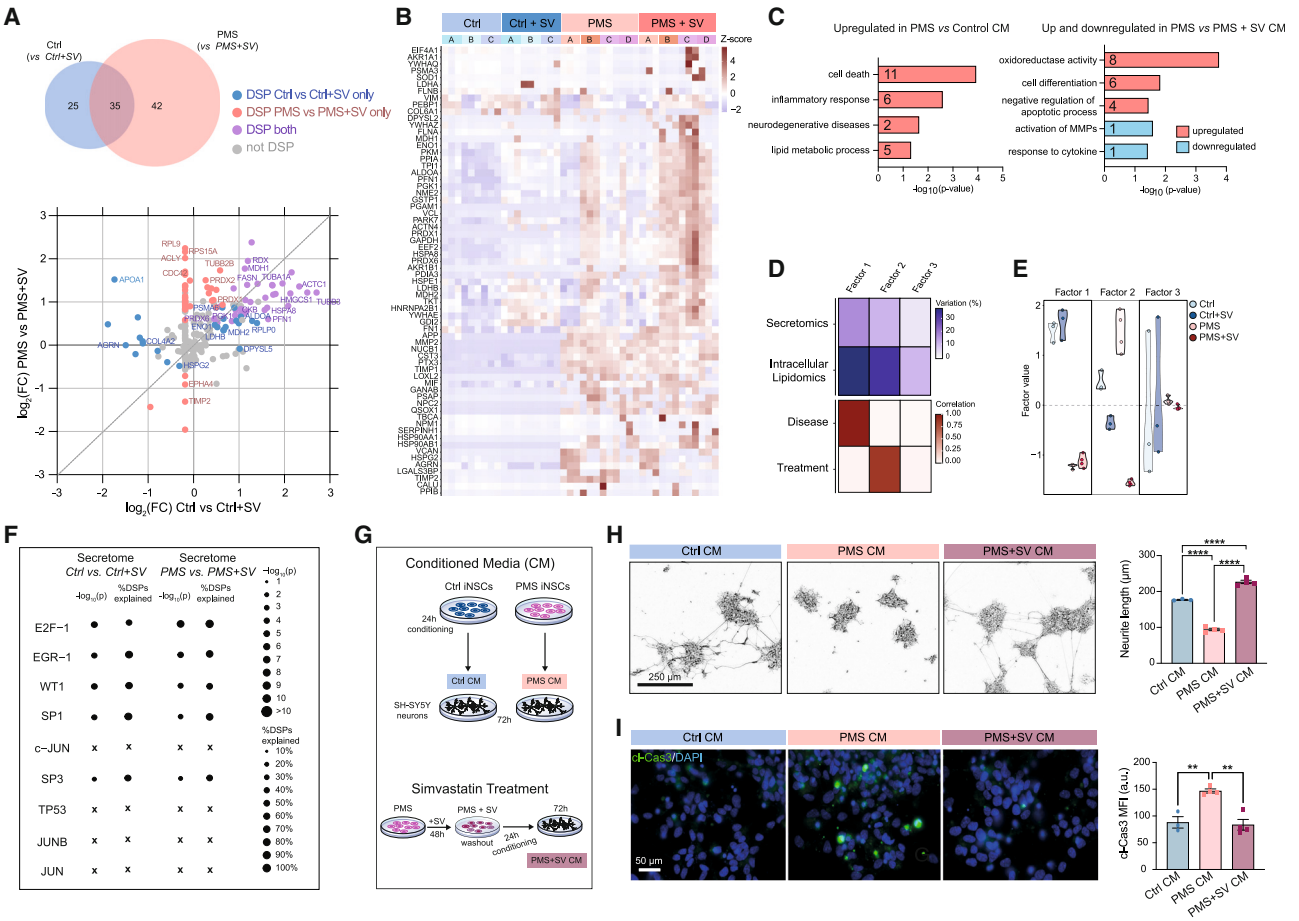


**Figure 5. HMGCR pharmacological inhibition rescues the neurotoxic SASP of PMS iNSC lines**

(A) Venn diagram and cross plot of DSPs in non-treated and SV-treated groups of both PMS and Ctrl iNSC lines. $Log_2$(FC) is reported for each comparison.

(B) Heatmap of SASP factors based on relative z-scores.

(C) Enrichment terms based on SASP factors identified in (B). Values represent number of SASP factors pertaining to the term.

(D) MOFA of secretomics and intracellular lipidomics and correlation for calculated factors separated by disease or treatment.

(E) Distribution of factor values within groups and by factors.

(F) TF enrichment analysis based on identified DSPs and proportion of total DSPs explained by each TF term, as in (A). TF term enrichment was considered significant at adjusted $p \leq 0.05$ under the hypergeometric test. X represents TF terms not differentially enriched.

(G) Experimental schematic of CM treatment paradigms.

(H) Representative phase contrast microscopy images and quantification of neurite length as in (G). Scale bar: 250 µm.

(I) Representative epifluorescence microscopy images and quantification of cl-Cas3 expression as in (G). Scale bar: 50 µm.

Experiments were done on $n = 3$ Ctrl and $n = 4$ PMS iNSC lines, each performed in $n \geq 3$ replicates. DSPs in (A)–(F) were considered significant at adjusted $p$ value $\leq 0.1$ (Benjamini-Hochberg correction) and $|log_2FC| > 0.2$ under the edgeR test. Differentially abundant lipids in (D) and (E) were considered significant at adjusted $p$ value $\leq 0.05$ (Benjamini-Hochberg correction) under Welch's t test. Data in (H) and (I) are mean values ± SEM. $^{**}p \leq 0.01$, $^{****}p \leq 0.0001$, one-way ANOVA with Tukey's multiple comparisons.

associated with EPH-ephrin signaling, ECM degradation, ROS detoxification, and apoptosis modulation (Figure S5B; Table S5). Several pathways upregulated in the PMS secretome were further upregulated after SV treatment, including pathways involved in axon guidance (e.g., L1CAM interactions, signaling by Rho GTPases). These enrichments were on account of new DSPs (Figures 5A and S5A), suggesting that the secretome may have acquired new functionalities following SV treatment.

Ctrl + SV-induced DSPs related to axon guidance and glycolysis but not cytoprotective mechanisms (Figure S5B). Treatment with SV further enhanced DSPs associated with cholesterol biosynthesis and glucose metabolism both in Ctrl and PMS iNSC lines, suggesting a shared compensatory mechanism, which has been previously reported using statins.[58]

Subsequently, we explored SASP-associated factors in the CMs of Ctrl, PMS, and SV-treated iNSC lines, utilizing the "*SASP Atlas*" proteomic database (Figure 5B).[46] Our analysis revealed an upregulation of SASP factors linked to cell death and inflammatory responses in PMS CMs vs. Ctrl CMs (Figure 5C). Treatment of PMS iNSC lines with SV upregulated SASP factors involved in oxidoreductase activity and cell differentiation while downregulating those associated with cytokine responses (Figure 5C).

Statins can exhibit dual effects on senescence depending on the cellular context.[59] We assessed the impact of SV treatment on SPiDER-β-gal expression as well as senescence-related genes and did not observe changes in senescence expression (Figures S5C and S5D). In addition, blocking the LXR pathway did not alter senescence gene expression after 48 h (Figure S5D). We also investigated whether SV treatment for 48 h was able to mitigate the hypermetabolic phenotype and glucose utilization in PMS iNSCs, revealing no differences in the Seahorse mitochondrial stress test (Figures S5E and S5F).

Collectively, our findings suggest a common compensatory response to HMGCR inhibition in both Ctrl and PMS iNSC lines. However, SV treatment reshapes the PMS iNSC SASP by promoting cytoprotective qualities. In addition, our assessment of senescence expression and metabolic parameters following SV treatment indicated no significant alterations, highlighting the independent effects of SV/HMGCR inhibition on the PMS iNSC SASP, senescence, and hypermetabolic state.

To integrate and summarize the observed variation between experimental groups across modalities (intracellular lipidomics and secretomics), we applied multi-omics factor analysis (MOFA).[60] The MOFA model was used to fit latent factors on the intracellular lipidome ($n$ = 642) and secretome ($n$ = 241) from untreated and SV-treated Ctrl and PMS iNSC lines. The total percentage of variance explained by the factors was higher in the lipidome dataset than in the secretome dataset across all factors, likely due in part to the larger number of features in this modality (Figure 5D). Factors 1 and 2 explained a non-negligible percentage of variance in both -omic views and thus could be seen as factors that are common to both lipidome and secretome modalities. Together, they explain 70.8% and 27.7% of the total variance in the lipidome and secretome modalities, respectively. To link factors 1 and 2 to disease state and treatment, we then assessed the relationship among the factors and the experimental groups (Figures 5D and 5E).

Factor 1 was found to be strongly correlated with the disease state (Ctrl or PMS), which we identified as a major driver of variation, and did not discriminate between untreated and SV-treated cell lines (Figures 5C and 5D). Factor 1 loadings in the lipidome modality showed high weights for lipid species previously identified as nonreactive to SV treatment, as well as an enrichment in saturated acyl groups that are not involved in cholesterol esterification (Figure S5G). Factor 1 loadings in the secretome modality showed high weights for DSPs between Ctrl and PMS iNSC lines, which were unaffected by SV treatment (Figure S5H), suggesting that these secretory features are unlikely to be regulated by the HMGCR-mediated lipogenic state of PMS iNSC lines. Instead, factor 2 was strongly associated with the SV treatment state (Figures 5D and 5E). This also captured the strong response to SV by PMS iNSCs compared with Ctrl iNSC lines. Factor 2 loadings in the lipidome modality showed high weights for lipid species whose reactivity we previously identified as modified in response to SV treatment (Figures 3E and S5C). Factor 2 loadings for the secretome modality showed high weights for DSPs between PMS and control iNSC lines corrected by SV treatment (e.g., EPHA4 and PRDX2) and DSPs *de novo* induced by SV treatment in PMS iNSC lines (e.g., HMGCS1 and FASN) (Figure S5J), suggesting that these secretory features are likely regulated by the HMGCR-mediated hyper-lipogenic state of PMS iNSC lines.

We next performed TF enrichment analysis using the DSPs from Ctrl vs. Ctrl + SV iNSCs and from PMS vs. PMS + SV iNSC lines. We identified E2F1, EGR1, WT1, SP1, and SP3 as top enriched candidates, which account for most of the secretory signatures mediated by SV treatment in Ctrl and PMS iNSC lines (Figure 5F). Taken together, our results suggest that the HMGCR-mediated hyper-lipogenic state of PMS iNSC lines regulates their secretory profile via transcriptional regulation by cholesterol-dependent TFs.

We hypothesized that increased DSPs/SASP factors related to cell death and inflammatory responses in the CMs of PMS iNSC lines would induce a response on mature neurons. To functionally validate these data, we exposed mature SH-SY5Y neurons to the CMs of Ctrl or PMS iNSC lines for 72 h (Figure 5G). We found that treatment of mature SH-SY5Y neurons to the CMs of PMS iNSC lines induced neurite retraction and apoptosis by measuring cleaved caspase-3 (cl-Cas3) expression in comparison with CMs of Ctrl iNSC lines (Figures 5H and 5I). CMs from PMS + SV prevented neurite retraction and apoptosis of the SH-SY5Y neurons (Figures 5G and 5H). Altogether, our findings suggest that inhibition of HMGCR by SV treatment prevents the induction of a neurotoxic SASP in PMS iNSC lines.

Pathway analysis identified DSPs related with EPH-ephrin signaling and ECM degradation, both of which were corrected by SV treatment. To investigate the role of ephrin signaling in neurotoxicity, we focused on EphA4, a significant candidate from our proteomic analysis. We used a blocking antibody for EphA4 in the CMs before treating mature SH-SY5Y neurons with CMs from Ctrl or PMS iNSC lines, as shown in Figures 5G–5I. Our results indicated that blocking EphA4 in the CMs from PMS iNSC lines did not prevent neurite loss when comparing PMS CMs + immunoglobulin G (IgG) to PMS CMs + EphA4 fragment crystallizable region (Fc), and it did not save the neurons from cell death (Figures S5K and S5L). Additionally, there was no significant difference in neurite length between Ctrl CMs + IgG and PMS CMs + EphA4 Fc, suggesting that the EphA4 blocking antibody had a minimal effect on neurite length in PMS CMs (Figure S5K). This implies that the neurotoxic effects seen in neurons are not caused by EphA4 alone but rather by a combination of different factors.

Overall, our work identifies a key role for cholesterol synthesis in controlling a disease-associated, lipid-related phenotype of PMS iNSC lines that leads to neurotoxic signaling and is rescuable.

## DISCUSSION

Here we leveraged direct reprogramming technology for a novel patient stem cell-derived model of MS and generated directly reprogrammed iNSCs from people with PMS, maintaining aging-associated epigenetic hallmarks.[17] We identified upregulation of senescence markers in the iPS-NSCs and iNSCs derived from people with PMS, in line with previously published work.[18,61] These results support genome-wide association studies data proposing an effect of genetic variants in genes associated with cellular senescence, mitochondrial function, and synaptic plasticity in glial cells.[15,16]

Our findings suggest that senescent PMS iNSCs sustain a hypermetabolic state, associated with increased glycolysis and

oxidative phosphorylation, accumulation of lipids, and SASP. Similar results have been reported in erythrocytes,[19] fibroblasts,[20,62] and astrocytes[21] of people with MS and in senescent cells,[23] without the identification of a clear function of this metabolic state in a pathophysiological context. We hypothesized that the cell-intrinsic senescent state in PMS iNSCs may be driving the hypermetabolism leading to lipid accumulation and the neurotoxic SASP. In PMS lesions, senescent, lipid-laden RG-like/NSCs may contribute to neurodegeneration via their neurotoxic SASP, promoting disease pathology.

Our results are in line with a growing body of evidence linking hypermetabolism to significant accumulation of LDs both in the context of senescence[25] as well as under physiological conditions in proliferative rodent NSCs.[24] Similar findings of FA trafficking between LDs and phospholipid pools have been reported in the context of lipid membrane restructuring in cellular stress responses.[63] Furthermore, LXR activation has been shown to drive cholesterol-induced senescence and neurodegeneration in macrophages.[64]

Similar lipidomic signatures, including changes in cholesterols and FAs, are being used as biomarkers of disease activity and progression in PMS.[65,66] Elevated levels of circulating cholesterol in the cerebrospinal fluid have been associated with adverse clinical and MRI outcomes in MS, suggesting a link between cholesterol synthesis and neuroinflammation.[67] It is however unknown whether increased circulating cholesterol is due to myelin destruction or is a by-product generated from CNS-infiltrating or -resident inflammatory cells. Biological changes in lipid species have also been broadly identified as a shared hallmark of neurodegenerative diseases, aging, and inflammatory conditions, such as viral infection.[68] However, the mechanisms underpinning these changes as well as their pathophysiological implications are incompletely understood.

We uncover a dichotomic effect of SV treatment in relation to the basal metabolic state of iNSCs, incurring a high phenotypic response of lipid-laden PMS iNSCs and a comparative insensitivity of controls. Accordingly, SV may in turn be targeting and metabolically reprogramming cells with high lipid anabolism in the CNS, which may include RG-like cells/NSCs, along with astrocytes and microglia. SV has gone through a phase-II clinical trial (MS-STAT) for PMS, showing attenuated brain atrophy and disease progression in patients through a yet unclear mechanism.[69] A recent investigation employed causal models to elucidate the mechanism of action of SV in the context of PMS and found the beneficial effects of SV to be independent of its effect on lowering peripheral cholesterol levels.[70]

Using multi-omics integration, we identified a secreted signature transcriptionally co-regulated by cholesterol-dependent TFs. The activity of several of the top identified TFs is known to be metabolically modulated by processes targeted by SV treatment in PMS iNSCs: the cholesterol metabolite itself,[52–54] the metabolic pathways of cholesterol synthesis,[55] cholesterol esterification,[56] and FA saturation.[57] We found that reshaping the PMS iNSC SASP with SV occurs independently of directly influencing the inherent senescent state. Similarly, a previous study examining cellular senescence observed an increase in multiple cholesterol metabolism proteins. Here, cholesterol depletion lowered expression of multiple SASP factors, while cholesterol repletion increased the SASP without influencing other markers of senescence.[71] These results highlight the intricate complexities and heterogeneity of the "senescent phenotype" and the need to reassess the defining traits of this broadly used term in a context-dependent manner.

In the PMS iNSC secretome, we observed an increase in ECM and ephrin-related molecules. TIMP1 has been linked to protective effects in MS by promoting oligodendrocyte progenitor cell differentiation.[72,73] Conversely, TIMP1 has been associated with promoting neuronal death and reducing neurite length, both *in vivo* and *in vitro*.[74,75] In MS, elevated MMP activity and decreased TIMP levels are believed to contribute to blood-brain barrier breakdown, although the specific roles of these proteins in the neurodegenerative aspects of the disease remain unclear. Senescent cells are known for secreting proteins involved in extracellular remodeling, including TIMPs and MMPs, which could potentially disrupt the balance of ECM molecules and lead to microenvironment dysfunction.[76] MS lesions have been found to express increased ephrin ligands and receptors, along with increased ECM molecules, believed to take part in the chronic neuroinflammation and neurodegeneration found in MS.[77,78] We investigated EphA4, a top hit identified in the proteomic screen, which has also been implicated in driving neurodegeneration in a plethora of neurological disorders, including Alzheimer's disease,[79] Parkinson's disease,[80] amyotrophic lateral sclerosis, and spinal muscular atrophy.[81] The neurotoxic effects seen in PMS iNSC CMs treated neurons are not caused by EphA4 alone but rather by a combination of reduced cytoprotective factors and increased inflammatory factors. It is reasonable to hypothesize that this newly identified PMS NSC secretory profile may trigger inflammatory and neurodegenerative responses in other neuronal and non-neuronal cell types found in the MS brain, which we have yet to investigate.

Overall, our data support the use of direct reprogramming technology to uncover new aging-associated cellular mechanisms of disease in PMS. By uncovering inherent dysfunction within stem cells derived from patients, our research also lays pivotal groundwork for critically assessing autologous stem cell therapies in MS. This underscores the potential for these patient-specific cells to carry distinct disease traits and internal dysfunctions, urging a reconsideration of their use in treatment approaches.[82]

## Limitations of the study

Compared with most stem cell-based disease modeling approaches for monogenic diseases, our study lacks a classical direct control given by isogenic lines, something that is at present not feasible for MS research. Given that we generated cell lines from individuals with possibly different genetic backgrounds, our study may also be falling short in study power to identify more subtle yet pathologically relevant features. We acknowledge the age differences between our cell lines. We added controls to mitigate this shortcoming, including the profiling of the starting fibroblasts and iPSCs. We also observe no phenotypic differences within our control lines corresponding to their age. While being very systematic in the characterization of paracrine mechanisms of cellular toxicity and injury, our work is not addressing the yet relevant question of whether the identified disease-associated dysfunctional cellular phenotype may also affect cell-to-cell interactions. Hence, multicellular 2D

and/or 3D cultures refined around the study of interactions between NSCs and neuronal vs. non-neuronal cells hold the promise to further understand the role and function of disease-associated NSCs in PMS.

## RESOURCE AVAILABILITY

### Lead contact

Further information and requests for resources and reagents should be directed to and will be fulfilled by the lead contact, Stefano Pluchino (spp24@cam.ac.uk).

### Materials availability

This study did not generate new unique reagents.

### Data and code availability

- Proteomics data have been deposited onto MassIVE:MSV000095283.
- The metabolomics (steady-state and stable isotope tracing) and lipidomics data described in this study are available at the NIH Common Fund's National Metabolomics Data Repository (NMDR) website, the Metabolomics Workbench, https://www.metabolomicsworkbench.org with the following Study IDs: Metabolomics Workbench: ST003331, ST003332, ST003328, ST003330.
- All original code has been deposited at Zenodo: https://doi.org/10.5281/zenodo.13764808 as of the date of publication.
- Any additional information required to reanalyze the data reported in this paper is available from the lead contact upon request.

## ACKNOWLEDGMENTS

The authors wish to acknowledge L. Ionescu, V. Pappa, G. Pluchino, O. Hruba, D. Sastre-Stanescu, M. Sciacovelli, A. Speed, A. Tolkovsky, D. Nerguizian, and F. Gamboni for technical and intellectual inputs throughout this study. The authors also thank M. Whitehead for providing the SH-SY5Y cells and the current and previous members of the Pluchino laboratory who have inspired or indirectly contributed to this work.

This research was supported by the Ferblanc Foundation G112716 (S.P. and A.M.N.); Catalyst Award from the UK MS Society H160 (S.P. and C.M.W.); National MS Society Research Grant RG 1802-30200 (S.P. and L.P.-J.); Bascule Charitable Trust RG98181 (S.P.); Wings for Life RG 82921 (S.P. and L.P.-J.); and the Fondazione Italiana Sclerosi Multipla FIMS 2018/R/14 (S.P. and L.P.-J.) and 2022/R-Single/011 (S.P. and A.M.N.). R.-B.I. is supported through an MRC-DTP and Cambridge Trust studentship and consumable award (RG86932) and St. Edmund's College Tutorial Award. A.M.N. is the recipient of a European Committee for Treatment and Research in Multiple Sclerosis (ECTRIMS) Postdoctoral Research Fellowship Exchange Program fellowship (G104956) and is supported through a UK MS Society Centre Excellence grant (G118541). E.C.W. is supported through an MRC-DTP iCASE PhD studentship award, jointly funded by AstraZeneca (G117817). I.M. is supported by Wellcome Trust (203151/Z/16/Z) and the UKRI Medical Research Council (MC_PC_17230). P.P. is supported through an MRC-DTP and Cambridge Trust PhD studentship and consumable award (RG86932) and Queen's College Tutorial Award. C.M.W. is the recipient of a National MS Society (USA) Post-doctoral fellowship (FG-2008-36954). L.P.-J. was supported by a Fondazione Italiana Sclerosi Multipla FIMS and Italian Multiple Sclerosis Association AISM Senior research fellowship financed or co-financed with the "5 per mille" public funding cod. 2017/B/5 (L.P.-J.), a Wellcome Trust Clinical Research Career Development Fellowship (G105713), and a National MS Society Research Grant RFA-2203-39318. F.E. is supported through the Austrian Science Fund (FWF) (Special Research Programme F7804-B; I 4791; TAI 801) and EJP European Joint Programme on Rare Diseases (I 5184).

## AUTHOR CONTRIBUTIONS

Conceptualization, R.-B.I., A.M.N., C.F., A.D., and S.P.; methodology, R.-B.I., A.M.N., J.A.R., E.C.W., P.P., C.M.W., M.D., D.S., M.S.C., S.R., L.P., L.P.-J., C.F., I.M., A.D., and S.P.; investigation, R.B.-I., A.M.N., J.A.R., E.C.W., P.P., C.M.W., M.B.C.S.-A., L.S., M.D., D.S., and L.P.; writing – original draft, R.B.-I. and A.M.N.; writing – review & editing, R.-B.I., A.M.N., J.A.R., E.C.W., C.M.W., L.P.-J., I.M., A.D., and S.P.; funding acquisition, R.-B.I., A.M.N., P.P., C.M.W., L.P.-J., I.M., A.D., and S.P.; resources, M.S.C., S.R., V.F., F.E., and T.L.; supervision, C.F., I.M., A.D., and S.P.

## DECLARATION OF INTERESTS

S.P. is founder, CSO, and shareholder (>5%) of CITC Ltd. A.D. is a founder of Omix Technologies Inc, Altis Biosciences LLC, and an advisory board member for Hemanext Inc and Macopharma Inc.

## STAR★METHODS

Detailed methods are provided in the online version of this paper and include the following:

- KEY RESOURCES TABLE
- EXPERIMENTAL MODEL AND SUBJECT DETAILS
  - Derivation and reprogramming of skin fibroblasts to iPSCs and iNSCs
- METHOD DETAILS
  - Trilineage Differentiation
  - RNA Isolation, RT-PCR, and qRT-PCR
  - Immunocytochemistry for iNSCs, iPSCs, and Trilineage Differentiation
  - SPiDER-β Galactosidase Detection by Flow Cytometry
  - Immunoblotting
  - Immunocytochemistry for mitochondrial morphology assay
  - Seahorse mitochondrial stress test
  - Cell size, mitochondrial mass, and membrane potential
  - Mitochondrial superoxide levels
  - Mitochondrial copy number assay
  - Simvastatin activation
  - Cytotoxicity Assay
  - Immunocytochemistry for lipid droplet quantification
  - High resolution imaging and 3D reconstruction of lipid droplets
  - Sample generation for metabolomics, stable isotope tracing, proteomics, and lipidomics
  - Sample processing for metabolomics and stable isotope tracing
  - Sample processing for proteomics analysis
  - Proteomics data acquisition
  - Proteomics Database Searching and Protein Identification - *Cells*
  - Database Searching and Protein Identification – *Conditioned media*
  - Protein acetylation
  - Lipidomics sample processing
  - Metabolomic and lipidomic analysis
  - Proteomics analysis
  - Multi-omics factor analysis (MOFA)
  - Multi-omics covariation network analysis
  - SH-SY5Y in vitro cultures, neuronal differentiation
  - Generation of iNSC conditioned media for treatments
  - Apoptosis assay
  - Assessment of neurite length
- QUANTIFICATION AND STATISTICAL ANALYSIS

## SUPPLEMENTAL INFORMATION

Supplemental information can be found online at https://doi.org/10.1016/j.stem.2024.09.014.

Received: February 12, 2024
Revised: August 1, 2024
Accepted: September 18, 2024
Published: October 21, 2024

## REFERENCES


1. Walton, C., King, R., Rechtman, L., Kaye, W., Leray, E., Marrie, R.A., Robertson, N., La Rocca, N., Uitdehaag, B., van der Mei, I., et al. (2020). Rising prevalence of multiple sclerosis worldwide: Insights from the Atlas of MS, third edition. Mult. Scler. *26*, 1816–1821. https://doi.org/10.1177/1352458520970841.
2. Lublin, F.D., Reingold, S.C., Cohen, J.A., Cutter, G.R., Sørensen, P.S., Thompson, A.J., Wolinsky, J.S., Balcer, L.J., Banwell, B., Barkhof, F., et al. (2014). Defining the clinical course of multiple sclerosis: The 2013 revisions. Neurology *83*, 278–286. https://doi.org/10.1212/wnl.0000000000000560.
3. Reich, D.S., Lucchinetti, C.F., and Calabresi, P.A. (2018). Multiple Sclerosis. N. Engl. J. Med. *378*, 169–180. https://doi.org/10.1056/NEJMra1401483.
4. Wilson, D.M., 3rd, Cookson, M.R., Van Den Bosch, L., Zetterberg, H., Holtzman, D.M., and Dewachter, I. (2023). Hallmarks of neurodegenerative diseases. Cell *186*, 693–714. https://doi.org/10.1016/j.cell.2022.12.032.
5. Scalfari, A. (2019). MS progression is predominantly driven by age-related mechanisms - YES. Mult. Scler. *25*, 902–904. https://doi.org/10.1177/1352458518820633.
6. Cole, J.H., Raffel, J., Friede, T., Eshaghi, A., Brownlee, W.J., Chard, D., De Stefano, N., Enzinger, C., Pirpamer, L., Filippi, M., et al. (2020). Longitudinal Assessment of Multiple Sclerosis with the Brain-Age Paradigm. Ann. Neurol. *88*, 93–105. https://doi.org/10.1002/ana.25746.
7. Tian, Y.E., Cropley, V., Maier, A.B., Lautenschlager, N.T., Breakspear, M., and Zalesky, A. (2023). Heterogeneous aging across multiple organ systems and prediction of chronic disease and mortality. Nat. Med. *29*, 1221–1231. https://doi.org/10.1038/s41591-023-02296-6.
8. Di Micco, R., Krizhanovsky, V., Baker, D., and d'Adda di Fagagna, F. (2021). Cellular senescence in ageing: from mechanisms to therapeutic opportunities. Nat. Rev. Mol. Cell Biol. *22*, 75–95. https://doi.org/10.1038/s41580-020-00314-w.
9. Herdy, J.R., Traxler, L., Agarwal, R.K., Karbacher, L., Schlachetzki, J.C.M., Boehnke, L., Zangwill, D., Galasko, D., Glass, C.K., Mertens, J., et al. (2022). Increased post-mitotic senescence in aged human neurons is a pathological feature of Alzheimer's disease. Cell Stem Cell *29*, 1637–1652.e6. https://doi.org/10.1016/j.stem.2022.11.010.
10. Idda, M.L., McClusky, W.G., Lodde, V., Munk, R., Abdelmohsen, K., Rossi, M., and Gorospe, M. (2020). Survey of senescent cell markers with age in human tissues. Aging (Albany, NY) *12*, 4052–4066. https://doi.org/10.18632/aging.102903.
11. Jessen, K.R., Mirsky, R., and Arthur-Farraj, P. (2015). The Role of Cell Plasticity in Tissue Repair: Adaptive Cellular Reprogramming. Dev. Cell *34*, 613–620. https://doi.org/10.1016/j.devcel.2015.09.005.
12. Sirko, S., Schichor, C., Della Vecchia, P., Metzger, F., Sonsalla, G., Simon, T., Bürkle, M., Kalpazidou, S., Ninkovic, J., Masserdotti, G., et al. (2023). Injury-specific factors in the cerebrospinal fluid regulate astrocyte plasticity in the human brain. Nat. Med. *29*, 3149–3161. https://doi.org/10.1038/s41591-023-02644-6.
13. Wu, D., Sun, J.K.L., and Chow, K.H.M. (2024). Neuronal cell cycle reentry events in the aging brain are more prevalent in neurodegeneration and lead to cellular senescence. PLoS Biol. *22*, e3002559. https://doi.org/10.1371/journal.pbio.3002559.
14. Absinta, M., Maric, D., Gharagozloo, M., Garton, T., Smith, M.D., Jin, J., Fitzgerald, K.C., Song, A., Liu, P., Lin, J.P., et al. (2021). A lymphocyte-microglia-astrocyte axis in chronic active multiple sclerosis. Nature *597*, 709–714. https://doi.org/10.1038/s41586-021-03892-7.
15. International; Multiple; Sclerosis; Genetics Consortium; MultipleMS Consortium (2023). Locus for severity implicates CNS resilience in progression of multiple sclerosis. Nature *619*, 323–331. https://doi.org/10.1038/s41586-023-06250-x.
16. Jokubaitis, V.G., Campagna, M.P., Ibrahim, O., Stankovich, J., Kleinova, P., Matesanz, F., Hui, D., Eichau, S., Slee, M., Lechner-Scott, J., et al. (2023). Not all roads lead to the immune system: the genetic basis of multiple sclerosis severity. Brain *146*, 2316–2331. https://doi.org/10.1093/brain/awac449.
17. Park, B., Nicaise, A., Tsitsipatis, D., Pirvan, L., Prasad, P., Novales, M.L.L.D., Whitten, J., Culig, L., Llewellyn, J., Ionescu, R.-B., et al. (2024). Integrative single-cell analysis of neural stem/progenitor cells reveals epigenetically dysregulated interferon response in progressive multiple sclerosis. Preprint at bioRxiv. https://doi.org/10.1101/2024.02.09.579648.
18. Nicaise, A.M., Wagstaff, L.J., Willis, C.M., Paisie, C., Chandok, H., Robson, P., Fossati, V., Williams, A., and Crocker, S.J. (2019). Cellular senescence in progenitor cells contributes to diminished remyelination potential in progressive multiple sclerosis. Proc. Natl. Acad. Sci. USA *116*, 9030–9039. https://doi.org/10.1073/pnas.1818348116.
19. Jacobs, M., Geiger, M., Summers, S., Janes, T., Boyea, R., Zinn, K., Aburashed, R., and Spence, D. (2022). Interferon-beta Decreases the Hypermetabolic State of Red Blood Cells from Patients with Multiple Sclerosis. ACS Chem. Neurosci. *13*, 2658–2665. https://doi.org/10.1021/acschemneuro.2c00332.
20. Wilkins, J.M., Gakh, O., Kabiraj, P., McCarthy, C.B., Tobin, W.O., Howe, C.L., and Lucchinetti, C.F. (2020). Signatures of cell stress and altered bioenergetics in skin fibroblasts from patients with multiple sclerosis. Aging (Albany, NY) *12*, 15134–15156. https://doi.org/10.18632/aging.103612.
21. Ghirotto, B., Oliveira, D.F., Cipelli, M., Basso, P.J., de Lima, J., Breda, C.N.S., Ribeiro, H.C., Silva, C.C.C., Sertié, A.L., Oliveira, A.E.R., et al. (2022). MS-Driven Metabolic Alterations Are Recapitulated in iPSC-Derived Astrocytes. Ann. Neurol. *91*, 652–669. https://doi.org/10.1002/ana.26336.
22. Bobba-Alves, N., Sturm, G., Lin, J., Ware, S.A., Karan, K.R., Monzel, A.S., Bris, C., Procaccio, V., Lenaers, G., Higgins-Chen, A., et al. (2023). Cellular allostatic load is linked to increased energy expenditure and accelerated biological aging. Psychoneuroendocrinology *155*, 106322. https://doi.org/10.1016/j.psyneuen.2023.106322.
23. Zahoor, I., Rui, B., Khan, J., Datta, I., and Giri, S. (2021). An emerging potential of metabolomics in multiple sclerosis: a comprehensive overview. Cell. Mol. Life Sci. *78*, 3181–3203. https://doi.org/10.1007/s00018-020-03733-2.
24. Ramosaj, M., Madsen, S., Maillard, V., Scandella, V., Sudria-Lopez, D., Yuizumi, N., Telley, L., and Knobloch, M. (2021). Lipid droplet availability affects neural stem/progenitor cell metabolism and proliferation. Nat. Commun. *12*, 7362. https://doi.org/10.1038/s41467-021-27365-7.
25. Hamsanathan, S., and Gurkar, A.U. (2022). Lipids as Regulators of Cellular Senescence. Front. Physiol. *13*, 796850. https://doi.org/10.3389/fphys.2022.796850.
26. Bocchi, R., Masserdotti, G., and Götz, M. (2022). Direct neuronal reprogramming: Fast forward from new concepts toward therapeutic approaches. Neuron *110*, 366–393. https://doi.org/10.1016/j.neuron.2021.11.023.
27. Erharter, A., Rizzi, S., Mertens, J., and Edenhofer, F. (2019). Take the shortcut - direct conversion of somatic cells into induced neural stem cells and their biomedical applications. FEBS Lett. *593*, 3353–3369. https://doi.org/10.1002/1873-3468.13656.
28. Nishihara, H., Perriot, S., Gastfriend, B.D., Steinfort, M., Cibien, C., Soldati, S., Matsuo, K., Guimbal, S., Mathias, A., Palecek, S.P., et al. (2022). Intrinsic blood-brain barrier dysfunction contributes to multiple sclerosis pathogenesis. Brain *145*, 4334–4348. https://doi.org/10.1093/brain/awac019.
29. Smith, M.D., Chamling, X., Gill, A.J., Martinez, H., Li, W., Fitzgerald, K.C., Sotirchos, E.S., Moroziewicz, D., Bauer, L., Paull, D., et al. (2022). Reactive Astrocytes Derived From Human Induced Pluripotent Stem Cells Suppress Oligodendrocyte Precursor Cell Differentiation. Front. Mol. Neurosci. *15*, 874299. https://doi.org/10.3389/fnmol.2022.874299.
30. Plastini, M.J., Desu, H.L., Ascona, M.C., Lang, A.L., Saporta, M.A., and Brambilla, R. (2022). Transcriptional abnormalities in induced pluripotent stem cell-derived oligodendrocytes of individuals with primary

progressive multiple sclerosis. Front. Cell. Neurosci. *16*, 972144. https://doi.org/10.3389/fncel.2022.972144.

31. Clayton, B.L.L., Barbar, L., Sapar, M., Kalpana, K., Rao, C., Migliori, B., Rusielewicz, T., NYSCF Global Stem Cell Array® Team, Paull, D., Brenner, K., et al. (2024). Patient iPSC models reveal glia-intrinsic phenotypes in multiple sclerosis. Published online August 25, 2024. Cell Stem Cell. https://doi.org/10.1016/j.stem.2024.08.002.
32. Meyer, S., Wörsdörfer, P., Günther, K., Thier, M., and Edenhofer, F. (2015). Derivation of Adult Human Fibroblasts and their Direct Conversion into Expandable Neural Progenitor Cells. J. Vis. Exp. *101*, e52831. https://doi.org/10.3791/52831.
33. Imm, J., Pishva, E., Ali, M., Kerrigan, T.L., Jeffries, A., Burrage, J., Glaab, E., Cope, E.L., Jones, K.M., Allen, N.D., et al. (2021). Characterization of DNA Methylomic Signatures in Induced Pluripotent Stem Cells During Neuronal Differentiation. Front. Cell Dev. Biol. *9*, 647981. https://doi.org/10.3389/fcell.2021.647981.
34. Thier, M., Wörsdörfer, P., Lakes, Y.B., Gorris, R., Herms, S., Opitz, T., Seiferling, D., Quandel, T., Hoffmann, P., Nöthen, M.M., et al. (2012). Direct conversion of fibroblasts into stably expandable neural stem cells. Cell Stem Cell *10*, 473–479. https://doi.org/10.1016/j.stem.2012.03.003.
35. De Cecco, M., Ito, T., Petrashen, A.P., Elias, A.E., Skvir, N.J., Criscione, S.W., Caligiana, A., Brocculi, G., Adney, E.M., Boeke, J.D., et al. (2019). L1 drives IFN in senescent cells and promotes age-associated inflammation. Nature *566*, 73–78. https://doi.org/10.1038/s41586-018-0784-9.
36. Kandhaya-Pillai, R., Miro-Mur, F., Alijotas-Reig, J., Tchkonia, T., Kirkland, J.L., and Schwartz, S. (2017). TNFalpha-senescence initiates a STAT-dependent positive feedback loop, leading to a sustained interferon signature, DNA damage, and cytokine secretion. Aging (Albany, NY) *9*, 2411–2435. https://doi.org/10.18632/aging.101328.
37. Wiley, C.D., and Campisi, J. (2021). The metabolic roots of senescence: mechanisms and opportunities for intervention. Nat. Metab. *3*, 1290–1301. https://doi.org/10.1038/s42255-021-00483-8.
38. Williams, N.C., and O'Neill, L.A.J. (2018). A Role for the Krebs Cycle Intermediate Citrate in Metabolic Reprogramming in Innate Immunity and Inflammation. Front. Immunol. *9*, 141. https://doi.org/10.3389/fimmu.2018.00141.
39. Bilotta, M.T., Petillo, S., Santoni, A., and Cippitelli, M. (2020). Liver X Receptors: Regulators of Cholesterol Metabolism, Inflammation, Autoimmunity, and Cancer. Front. Immunol. *11*, 584303. https://doi.org/10.3389/fimmu.2020.584303.
40. Chu, K., Miyazaki, M., Man, W.C., and Ntambi, J.M. (2006). Stearoyl-coenzyme A desaturase 1 deficiency protects against hypertriglyceridemia and increases plasma high-density lipoprotein cholesterol induced by liver X receptor activation. Mol. Cell. Biol. *26*, 6786–6798. https://doi.org/10.1128/MCB.00077-06.
41. Zhu, R., Ou, Z., Ruan, X., and Gong, J. (2012). Role of liver X receptors in cholesterol efflux and inflammatory signaling (review). Mol. Med. Rep. *5*, 895–900. https://doi.org/10.3892/mmr.2012.758.
42. Rose, T.D., Köhler, N., Falk, L., Klischat, L., Lazareva, O.E., and Pauling, J.K. (2023). Lipid network and moiety analysis for revealing enzymatic dysregulation and mechanistic alterations from lipidomics data. Brief. Bioinform. *24*, bbac572. https://doi.org/10.1093/bib/bbac572.
43. Gaud, C., C Sousa, B., Nguyen, A., Fedorova, M., Ni, Z., O'Donnell, V.B., Wakelam, M.J.O., Andrews, S., and Lopez-Clavijo, A.F. (2021). BioPAN: a web-based tool to explore mammalian lipidome metabolic pathways on LIPID MAPS. F1000Res *10*, 4. https://doi.org/10.12688/f1000research.28022.2.
44. Coppé, J.P., Patil, C.K., Rodier, F., Krtolica, A., Beauséjour, C.M., Parrinello, S., Hodgson, J.G., Chin, K., Desprez, P.Y., and Campisi, J. (2010). A human-like senescence-associated secretory phenotype is conserved in mouse cells dependent on physiological oxygen. PLoS One *5*, e9188. https://doi.org/10.1371/journal.pone.0009188.
45. Özcan, S., Alessio, N., Acar, M.B., Mert, E., Omerli, F., Peluso, G., and Galderisi, U. (2016). Unbiased analysis of senescence associated secretory phenotype (SASP) to identify common components following different genotoxic stresses. Aging (Albany, NY) *8*, 1316–1329. https://doi.org/10.18632/aging.100971.
46. Basisty, N., Kale, A., Jeon, O.H., Kuehnemann, C., Payne, T., Rao, C., Holtz, A., Shah, S., Sharma, V., Ferrucci, L., et al. (2020). A proteomic atlas of senescence-associated secretomes for aging biomarker development. PLoS Biol. *18*, e3000599. https://doi.org/10.1371/journal.pbio.3000599.
47. Lehmann, B.D., Paine, M.S., Brooks, A.M., McCubrey, J.A., Renegar, R.H., Wang, R., and Terrian, D.M. (2008). Senescence-associated exosome release from human prostate cancer cells. Cancer Res. *68*, 7864–7871. https://doi.org/10.1158/0008-5472.CAN-07-6538.
48. Salotti, J., and Johnson, P.F. (2019). Regulation of senescence and the SASP by the transcription factor C/EBPβ. Exp. Gerontol. *128*, 110752. https://doi.org/10.1016/j.exger.2019.110752.
49. Potluri, S., Assi, S.A., Chin, P.S., Coleman, D.J.L., Pickin, A., Moriya, S., Seki, N., Heidenreich, O., Cockerill, P.N., and Bonifer, C. (2021). Isoform-specific and signaling-dependent propagation of acute myeloid leukemia by Wilms tumor 1. Cell Rep. *35*, 109010. https://doi.org/10.1016/j.celrep.2021.109010.
50. Lee, T.H., Moffett, P., and Pelletier, J. (1999). The Wilms' tumor suppressor gene (wt1) product represses different functional classes of transcriptional activation domains. Nucleic Acids Res. *27*, 2889–2897. https://doi.org/10.1093/nar/27.14.2889.
51. Dejong, V., Degeorges, A., Filleur, S., Ait-Si-Ali, S., Mettouchi, A., Bornstein, P., Binétruy, B., and Cabon, F. (1999). The Wilms' tumor gene product represses the transcription of thrombospondin 1 in response to overexpression of c-Jun. Oncogene *18*, 3143–3151. https://doi.org/10.1038/sj.onc.1202654.
52. Loats, A.E., Carrera, S., Fleming, A.F., Roberts, A.R.E., Sherrard, A., Toska, E., Moorhouse, A.J., Medler, K.F., and Roberts, S.G.E. (2021). Cholesterol is required for transcriptional repression by BASP1. Proc. Natl. Acad. Sci. USA *118*, e2101671118. https://doi.org/10.1073/pnas.2101671118.
53. Scheinman, E.J., Rostoker, R., and Leroith, D. (2013). Cholesterol affects gene expression of the Jun family in colon carcinoma cells using different signaling pathways. Mol. Cell. Endocrinol. *374*, 101–107. https://doi.org/10.1016/j.mce.2013.04.011.
54. Pan, Z., Wang, K., Wang, X., Jia, Z., Yang, Y., Duan, Y., Huang, L., Wu, Z.X., Zhang, J.Y., and Ding, X. (2022). Cholesterol promotes EGFR-TKIs resistance in NSCLC by inducing EGFR/Src/Erk/SP1 signaling-mediated ERRalpha re-expression. Mol. Cancer *21*, 77. https://doi.org/10.1186/s12943-022-01547-3.
55. Cai, J.P., Chen, W., Hou, X., Liang, L.J., Hao, X.Y., and Yin, X.Y. (2013). Simvastatin enhances the chemotherapeutic efficacy of S-1 against bile duct cancer: E2F-1/TS downregulation might be the mechanism. Anticancer Drugs *24*, 1020–1029. https://doi.org/10.1097/CAD.0b013e328364f935.
56. Xiong, K., Wang, G., Peng, T., Zhou, F., Chen, S., Liu, W., Ju, L., Xiao, Y., Qian, K., and Wang, X. (2021). The cholesterol esterification inhibitor avasimibe suppresses tumour proliferation and metastasis via the E2F-1 signalling pathway in prostate cancer. Cancer Cell Int. *21*, 461. https://doi.org/10.1186/s12935-021-02175-5.
57. Vivas-García, Y., Falletta, P., Liebing, J., Louphrasitthiphol, P., Feng, Y., Chauhan, J., Scott, D.A., Glodde, N., Chocarro-Calvo, A., Bonham, S., et al. (2020). Lineage-Restricted Regulation of SCD and Fatty Acid Saturation by MITF Controls Melanoma Phenotypic Plasticity. Mol. Cell *77*, 120–137.e9. https://doi.org/10.1016/j.molcel.2019.10.014.
58. Jiang, S.Y., Li, H., Tang, J.J., Wang, J., Luo, J., Liu, B., Wang, J.K., Shi, X.J., Cui, H.W., Tang, J., et al. (2018). Discovery of a potent HMG-CoA reductase degrader that eliminates statin-induced reductase accumulation and lowers cholesterol. Nat. Commun. *9*, 5138. https://doi.org/10.1038/s41467-018-07590-3.
59. Ahmadi, Y., Fard, J.K., Ghafoor, D., Eid, A.H., and Sahebkar, A. (2023). Paradoxical effects of statins on endothelial and cancer cells: the impact of concentrations. Cancer Cell Int. *23*, 43. https://doi.org/10.1186/s12935-023-02890-1.

60. Argelaguet, R., Velten, B., Arnol, D., Dietrich, S., Zenz, T., Marioni, J.C., Buettner, F., Huber, W., and Stegle, O. (2018). Multi-Omics Factor Analysis-a framework for unsupervised integration of multi-omics data sets. Mol. Syst. Biol. *14*, e8124. https://doi.org/10.15252/msb.20178124.

61. Mutukula, N., Man, Z., Takahashi, Y., Iniesta Martinez, F., Morales, M., Carreon-Guarnizo, E., Hernandez Clares, R., Garcia-Bernal, D., Martinez Martinez, L., Lajara, J., et al. (2021). Generation of RRMS and PPMS specific iPSCs as a platform for modeling Multiple Sclerosis. Stem Cell Res. *53*, 102319. https://doi.org/10.1016/j.scr.2021.102319.

62. Wilkins, J.M., Gakh, O., Guo, Y., Popescu, B., Staff, N.P., and Lucchinetti, C.F. (2023). Biomolecular alterations detected in multiple sclerosis skin fibroblasts using Fourier transform infrared spectroscopy. Front. Cell. Neurosci. *17*, 1223912. https://doi.org/10.3389/fncel.2023.1223912.

63. Danielli, M., Perne, L., Jarc Jovičić, E., and Petan, T. (2023). Lipid droplets and polyunsaturated fatty acid trafficking: Balancing life and death. Front. Cell Dev. Biol. *11*, 1104725. https://doi.org/10.3389/fcell.2023.1104725.

64. Terao, R., Lee, T.J., Colasanti, J., Pfeifer, C.W., Lin, J.B., Santeford, A., Hase, K., Yamaguchi, S., Du, D., Sohn, B.S., et al. (2024). LXR/CD38 activation drives cholesterol-induced macrophage senescence and neurodegeneration via $NAD^+$ depletion. Cell Rep. *43*, 114102. https://doi.org/10.1016/j.celrep.2024.114102.

65. van de Kraats, C., Killestein, J., Popescu, V., Rijkers, E., Vrenken, H., Lütjohann, D., Barkhof, F., Polman, C.H., and Teunissen, C.E. (2014). Oxysterols and cholesterol precursors correlate to magnetic resonance imaging measures of neurodegeneration in multiple sclerosis. Mult. Scler. *20*, 412–417. https://doi.org/10.1177/1352458513499421.

66. Uher, T., Fellows, K., Horakova, D., Zivadinov, R., Vaneckova, M., Sobisek, L., Tyblova, M., Seidl, Z., Krasensky, J., Bergsland, N., et al. (2017). Serum lipid profile changes predict neurodegeneration in interferon-beta1a-treated multiple sclerosis patients. J. Lipid Res. *58*, 403–411. https://doi.org/10.1194/jlr.M072751.

67. Zhornitsky, S., McKay, K.A., Metz, L.M., Teunissen, C.E., and Rangachari, M. (2016). Cholesterol and markers of cholesterol turnover in multiple sclerosis: relationship with disease outcomes. Mult. Scler. Relat. Disord. *5*, 53–65. https://doi.org/10.1016/j.msard.2015.10.005.

68. Hornburg, D., Wu, S., Moqri, M., Zhou, X., Contrepois, K., Bararpour, N., Traber, G.M., Su, B., Metwally, A.A., Avina, M., et al. (2023). Dynamic lipidome alterations associated with human health, disease and ageing. Nat. Metab. *5*, 1578–1594. https://doi.org/10.1038/s42255-023-00880-1.

69. Chataway, J., Schuerer, N., Alsanousi, A., Chan, D., MacManus, D., Hunter, K., Anderson, V., Bangham, C.R.M., Clegg, S., Nielsen, C., et al. (2014). Effect of high-dose simvastatin on brain atrophy and disability in secondary progressive multiple sclerosis (MS-STAT): a randomised, placebo-controlled, phase 2 trial. Lancet *383*, 2213–2221. https://doi.org/10.1016/S0140-6736(13)62242-4.

70. Eshaghi, A., Kievit, R.A., Prados, F., Sudre, C.H., Nicholas, J., Cardoso, M.J., Chan, D., Nicholas, R., Ourselin, S., Greenwood, J., et al. (2019). Applying causal models to explore the mechanism of action of simvastatin in progressive multiple sclerosis. Proc. Natl. Acad. Sci. USA *116*, 11020–11027. https://doi.org/10.1073/pnas.1818978116.

71. Roh, K., Noh, J., Kim, Y., Jang, Y., Kim, J., Choi, H., Lee, Y., Ji, M., Kang, D., Kim, M.S., et al. (2023). Lysosomal control of senescence and inflammation through cholesterol partitioning. Nat. Metab. *5*, 398–413. https://doi.org/10.1038/s42255-023-00747-5.

72. Moore, C.S., Milner, R., Nishiyama, A., Frausto, R.F., Serwanski, D.R., Pagarigan, R.R., Whitton, J.L., Miller, R.H., and Crocker, S.J. (2011). Astrocytic tissue inhibitor of metalloproteinase-1 (TIMP-1) promotes oligodendrocyte differentiation and enhances CNS myelination. J. Neurosci. *31*, 6247–6254. https://doi.org/10.1523/JNEUROSCI.5474-10.2011.

73. Nicaise, A.M., Johnson, K.M., Willis, C.M., Guzzo, R.M., and Crocker, S.J. (2019). TIMP-1 Promotes Oligodendrocyte Differentiation Through Receptor-Mediated Signaling. Mol. Neurobiol. *56*, 3380–3392. https://doi.org/10.1007/s12035-018-1310-7.

74. Jourquin, J., Tremblay, E., Bernard, A., Charton, G., Chaillan, F.A., Marchetti, E., Roman, F.S., Soloway, P.D., Dive, V., Yiotakis, A., et al. (2005). Tissue inhibitor of metalloproteinases-1 (TIMP-1) modulates neuronal death, axonal plasticity, and learning and memory. Eur. J. Neurosci. *22*, 2569–2578. https://doi.org/10.1111/j.1460-9568.2005.04426.x.

75. Ould-Yahoui, A., Tremblay, E., Sbai, O., Ferhat, L., Bernard, A., Charrat, E., Gueye, Y., Lim, N.H., Brew, K., Risso, J.J., et al. (2009). A new role for TIMP-1 in modulating neurite outgrowth and morphology of cortical neurons. PLoS One *4*, e8289. https://doi.org/10.1371/journal.pone.0008289.

76. Levi, N., Papismadov, N., Solomonov, I., Sagi, I., and Krizhanovsky, V. (2020). The ECM path of senescence in aging: components and modifiers. FEBS J. *287*, 2636–2646. https://doi.org/10.1111/febs.15282.

77. Sobel, R.A. (2005). Ephrin A receptors and ligands in lesions and normal-appearing white matter in multiple sclerosis. Brain Pathol. *15*, 35–45. https://doi.org/10.1111/j.1750-3639.2005.tb00098.x.

78. van Horssen, J., Bö, L., Dijkstra, C.D., and de Vries, H.E. (2006). Extensive extracellular matrix depositions in active multiple sclerosis lesions. Neurobiol. Dis. *24*, 484–491. https://doi.org/10.1016/j.nbd.2006.08.005.

79. Vargas, L.M., Cerpa, W., Muñoz, F.J., Zanlungo, S., and Alvarez, A.R. (2018). Amyloid-beta oligomers synaptotoxicity: The emerging role of EphA4/c-Abl signaling in Alzheimer's disease. Biochim. Biophys. Acta Mol. Basis Dis. *1864*, 1148–1159. https://doi.org/10.1016/j.bbadis.2018.01.023.

80. Shi, M., Movius, J., Dator, R., Aro, P., Zhao, Y., Pan, C., Lin, X., Bammler, T.K., Stewart, T., Zabetian, C.P., et al. (2015). Cerebrospinal fluid peptides as potential Parkinson disease biomarkers: a staged pipeline for discovery and validation. Mol. Cell. Proteomics *14*, 544–555. https://doi.org/10.1074/mcp.M114.040576.

81. Zhao, J., Stevens, C.H., Boyd, A.W., Ooi, L., and Bartlett, P.F. (2021). Role of EphA4 in Mediating Motor Neuron Death in MND. Int. J. Mol. Sci. *22*, 9430. https://doi.org/10.3390/ijms22179430.

82. Pluchino, S., Smith, J.A., and Peruzzotti-Jametti, L. (2020). Promises and Limitations of Neural Stem Cell Therapies for Progressive Multiple Sclerosis. Trends Mol. Med. *26*, 898–912. https://doi.org/10.1016/j.molmed.2020.04.005.

83. Douvaras, P., and Fossati, V. (2015). Generation and isolation of oligodendrocyte progenitor cells from human pluripotent stem cells. Nat. Protoc. *10*, 1143–1154. https://doi.org/10.1038/nprot.2015.075.

84. Douvaras, P., Wang, J., Zimmer, M., Hanchuk, S., O'Bara, M.A., Sadiq, S., Sim, F.J., Goldman, J., and Fossati, V. (2014). Efficient generation of myelinating oligodendrocytes from primary progressive multiple sclerosis patients by induced pluripotent stem cells. Stem Cell Rep. *3*, 250–259. https://doi.org/10.1016/j.stemcr.2014.06.012.

85. Valente, A.J., Maddalena, L.A., Robb, E.L., Moradi, F., and Stuart, J.A. (2017). A simple ImageJ macro tool for analyzing mitochondrial network morphology in mammalian cell culture. Acta Histochem. *119*, 315–326. https://doi.org/10.1016/j.acthis.2017.03.001.

86. Nemkov, T., Reisz, J.A., Gehrke, S., Hansen, K.C., and D'Alessandro, A. (2019). High-Throughput Metabolomics: Isocratic and Gradient Mass Spectrometry-Based Methods. Methods Mol. Biol. *1978*, 13–26. https://doi.org/10.1007/978-1-4939-9236-2_2.

87. Nemkov, T., Hansen, K.C., and D'Alessandro, A. (2017). A three-minute method for high-throughput quantitative metabolomics and quantitative tracing experiments of central carbon and nitrogen pathways. Rapid Commun. Mass Spectrom. *31*, 663–673. https://doi.org/10.1002/rcm.7834.

88. Dillies, M.A., Rau, A., Aubert, J., Hennequet-Antier, C., Jeanmougin, M., Servant, N., Keime, C., Marot, G., Castel, D., Estelle, J., et al. (2013). A comprehensive evaluation of normalization methods for Illumina high-throughput RNA sequencing data analysis. Brief. Bioinform. *14*, 671–683. https://doi.org/10.1093/bib/bbs046.

89. Moutsopoulos, I., Williams, E.C., and Mohorianu, I.I. (2023). bulkAnalyseR: an accessible, interactive pipeline for analysing and sharing bulk multimodal sequencing data. Brief. Bioinform. *24*, bbac591. https://doi.org/10.1093/bib/bbac591.

90. Robinson, M.D., McCarthy, D.J., and Smyth, G.K. (2010). edgeR: a Bioconductor package for differential expression analysis of digital gene

expression data. Bioinformatics *26*, 139–140. https://doi.org/10.1093/bioinformatics/btp616.

91. Raudvere, U., Kolberg, L., Kuzmin, I., Arak, T., Adler, P., Peterson, H., and Vilo, J. (2019). g:Profiler: a web server for functional enrichment analysis and conversions of gene lists (2019 update). Nucleic Acids Res. *47*, W191–W198. https://doi.org/10.1093/nar/gkz369.
92. Huynh-Thu, V.A., Irrthum, A., Wehenkel, L., and Geurts, P. (2010). Inferring regulatory networks from expression data using tree-based methods. PLoS One *5*, e12776. https://doi.org/10.1371/journal.pone.0012776.
93. Meijering, E., Jacob, M., Sarria, J.C., Steiner, P., Hirling, H., and Unser, M. (2004). Design and validation of a tool for neurite tracing and analysis in fluorescence microscopy images. Cytometry A *58*, 167–176. https://doi.org/10.1002/cyto.a.20022.
94. Rohart, F., Gautier, B., Singh, A., and Lê Cao, K.A. (2017). mixOmics: An R package for 'omics feature selection and multiple data integration. PLoS Comput. Biol. *13*, e1005752. https://doi.org/10.1371/journal.pcbi.1005752.

## STAR★METHODS

### KEY RESOURCES TABLE

| REAGENT or RESOURCE | SOURCE | IDENTIFIER |
|---|---|---|
| Antibodies | | |
| Chicken anti Nestin | Novus Biolgicals | Cat#NB100-1604; RRID: AB_2282642 |
| Rabbit anti ETNPPL | Atlas | Cat#HPA044546; RRID: AB_10962867 |
| Rabbit anti SOX2 | Abcam | Cat#ab97959; RRID:AB_2341193 |
| Mouse anti SSEA4 | Thermo Fisher | Cat#41-4000; RRID:AB_2533506 |
| Rabbit anti Nanog | Abcam | Cat#ab21624; RRID:AB_446437 |
| Mouse anti Oct3/4 | Santa Cruz | Cat#sc-5279; RRID:AB_628051 |
| Goat anti SOX17 | R&D | Cat#AF1924; RRID:AB_355060 |
| Goat anti ACTA2 (α smooth muscle actin) | Antibodies.com | Cat#A82445; RRID:AB_2747885 |
| Rabbit anti Pax6 | BioLegend | Cat#901302; RRID:AB_2749901 |
| Goat anti SOX1 | R&D | Cat#AF3369; RRID:AB_2239879 |
| Rabbit anti Oct4 | Reprocell | Cat#09-0023; RRID:AB_2167689 |
| Mouse anti TRA-1-60 | EMD Millipore | Cat#MAB4360; RRID:AB_2119183 |
| Mouse anti TRA-1-81 | EMD Millipore | Cat#MAB4381; RRID:AB_177638 |
| Rabbit anti NANOG | Cell Signaling | Cat#4903; RRID:AB_10829232 |
| Mouse anti SSEA4 | Abcam | Cat#ab16287; RRID:AB_778073 |
| Rabbit anti SOX2 | Reprocell | Cat#09-0024 (discontinued); RRID:AB_2195775 |
| Alexa Fluor 647-conjugated Rabbit anti-TOMM20 | Abcam | Cat#ab209606; RRID:AB_2934123 |
| Rabbit anti phospho-Stat1 (Tyr701) | Cell Signaling | Cat#7649; RRID:AB_10950970 |
| Rabbit anti Stat1 | Cell Signaling | Cat#9172; RRID:AB_2198300 |
| Rabbit anti ISG15 | Cell Signaling | Cat#2743; RRID:AB_2126201 |
| Rabbit anti Cleaved Caspase-3 (Asp175) | Cell Signaling | Cat#9664; RRID:AB_2070042 |
| Mouse anti β-Actin | Thermo Fisher | Cat#A1978; RRID:AB_476692 |
| Alexa Fluor 488-conjugated Goat Anti Chicken IgY | Thermo Fisher | Cat#A11039; RRID:AB_2534096 |
| Alexa Fluor 546-conjugated Goat Anti Rabbit IgG | Thermo Fisher | Cat#A11010; RRID:AB_2534077 |
| Alexa Fluor 488-conjugated Donkey Anti Rabbit IgG | Thermo Fisher | Cat#A21206; RRID:AB_2535792 |
| Alexa Fluor 488-conjugated Goat Anti Mouse IgM, IgG | Thermo Fisher | Cat#A10680; RRID:AB_2534062 |
| Alexa Fluor 546-conjugated Donkey Anti Goat IgG | Thermo Fisher | Cat#A11056; RRID:AB_2534103 |
| Alexa Fluor 647-conjugated Donkey Anti Goat IgG | Thermo Fisher | Cat#A21447; RRID:AB_141844 |
| Alexa Fluor 488-conjugated Goat Anti Rabbit IgG | Thermo Fisher | Cat#A11008; RRID:AB_143165 |
| Anti-mouse IgG, HRP-linked Antibody | Cell Signaling | Cat#7076; RRID:AB_330924 |
| Anti-rabbit IgG, HRP-linked Antibody | Cell Signaling | Cat#7074; RRID:AB_2099233 |
| SYTOX Blue | Thermo Fisher | Cat#S34857 |
| Human IgG Fc Antibody | R&D Systems | Cat#MAB110 |
| Recombinant Human EphA4 Fc Chimera Protein | R&D Systems | Cat#6827-A4-050 |
| Chemicals, peptides, and recombinant proteins | | |
| RPMI 1640 | Thermo Fisher | Cat#11875093 |
| Antibiotic-antimycotic (100X) | Thermo Fisher | Cat#15240062 |
| KnockOut DMEM | Thermo Fisher | Cat#10829018 |
| DMEM, high glucose | Thermo Fisher | Cat#11965092 |
| Trypsin-EDTA (0.05%) | Thermo Fisher | Cat#25300062 |
| mTeSR 1 | STEMCELL Technologies | Cat#85857 |
| hESC-Qualified Matrigel | Corning | Cat#354277 |
| Accutase | Thermo Fisher | Cat#A1110501 |
| Fluoromount-G | Thermo Fisher | Cat#00-4958-02 |

(*Continued on next page*)

*Continued*

| REAGENT or RESOURCE | SOURCE | IDENTIFIER |
|---|---|---|
| DAPI fluorescence reagent for DNA | Thermo Fisher | Cat#D8417 |
| Hoechst | Sigma Aldrich | Cat#94403 |
| DreamTaq Hot Start DNA Polymerase | Thermo Fisher | Cat#EP1702 |
| dNTP Mix (10 mM each) | Thermo Fisher | Cat#R0192 |
| Agarose | Scientific Laboratory Supplies | Cat#BIO41025 |
| TAE buffer, 50X | MP Biomedicals | Cat#11TAE50X01 |
| TrackIt 100bp DNA Ladder | Thermo Fisher | Cat#10488058 |
| Gel Loading Dye (6X) | New England BioLabs | Cat#B7024S |
| GelRed Nucleic Acid Gel Stain | Biotium | Cat#41003 |
| RIPA Lysis and Extraction Buffer | Abcam | Cat#ab156034 |
| Halt Protease & Phosphatase Inhibitor Cocktail | Thermo Fisher | Cat#1861281 |
| NuPAGE LDS Sample Buffer | Thermo Fisher | Cat#NP0007 |
| NuPAGE Sample Reducing Agent | Thermo Fisher | Cat#NP0009 |
| Tris/Glycine/SDS Buffer | Bio-Rad | Cat#1610732 |
| SeeBlue Plus2 Prestained Standard | Thermo Fisher | Cat# LC5925 |
| Bovine Serum Albumin | Thermo Fisher | Cat#1002096887 |
| Skim Milk Powder | Thermo Fisher | Cat#70166 |
| TBS Buffer | Thermo Fisher | Cat#28358 |
| TWEEN 20 | Thermo Fisher | Cat#102423676 |
| Triton X-100 | Thermo Fisher | Cat#1002575509 |
| Clarity Western ECL Substrate | Bio-Rad | Cat#170-5061 |
| Formaldehyde solution | Thermo Fisher | Cat#47608 |
| Normal goat serum | Thermo Fisher | Cat#16-210-064 |
| Normal donkey serum | Thermo Fisher | Cat# D9663 |
| LipidSpot 610 | Biotium | Cat#70069 |
| BioTracker 555 Orange Cytoplasmic Membrane Dye | Thermo Fisher | Cat#SCT107 |
| DMEM/F12 | Thermo Fisher | Cat#11320033 |
| DMEM/F12 w/o glucose | Elabscience | Cat#EP-CM-L0127-ELA |
| DMEM/F12 w/o glutamine | Thermo Fisher | Cat#21331020 |
| Neurobasal A Medium | Thermo Fisher | Cat#21103049 |
| GlutaMAX | Thermo Fisher | Cat#35050038 |
| B-27 Supplement | Thermo Fisher | Cat#17504044 |
| N-2 Supplement | Thermo Fisher | Cat#17502001 |
| CHIR99021 | Cell Guidance Systems | Cat#SM13 |
| hLIF | Cell Signaling Technology | Cat#62226S |
| SB-431542 | Cayman Chemicals | Cat#13031 |
| Y-27632 | Miltenyi Biotec | Cat#130-103-933 |
| All-Trans Retinoic Acid | STEMCELL Technologies | Cat#72262 |
| Growth Factor Reduced Matrigel Matrix | Corning | Cat#354230 |
| Seahorse XF calibrant solution | Agilent | Cat#100840-000 |
| XF DMEM medium | Agilent | Cat#103575-100 |
| XF 1.0 M glucose solution | Agilent | Cat#103577-100 |
| XF 100 mM pyruvate solution | Agilent | Cat#103578-100 |
| XF 200 mM glutamine solution | Agilent | Cat#103579-100 |
| MitoTracker Green | Thermo Fisher | Cat#M7514 |
| MitoTracker Red CMXRos | Thermo Fisher | Cat# M7512 |
| MitoSOX Red | Thermo Fisher | Cat# M36008 |
| D-Glucose-$^{13}C_6$ | Thermo Fisher | Cat#389374 |
| L-Glutamine-$^{13}C_5$,$^{15}N_2$ | Thermo Fisher | Cat#607983 |
| DMEM Glutamax I | Thermo Fisher | Cat#61965-026 |

(*Continued on next page*)

*Continued*

| REAGENT or RESOURCE | SOURCE | IDENTIFIER |
|---|---|---|
| Fetal Bovine Serum | Thermo Fisher | Cat#26-140-079 |
| MEM Non Essential Amino Acids Solution | Thermo Fisher | Cat#11-140-050 |
| Sodium pyruvate | Thermo Fisher | Cat#11530396 |
| Penicillin Streptomycin (P/S) | Thermo Fisher | Cat#15-140-122 |
| 2-Mercaptoethanol | Thermo Fisher | Cat#21985023 |
| DMSO | Sigma Aldrich | Cat#D2650 |
| KnockOut Serum Replacement | Thermo Fisher | Cat#10828028 |
| Cell Staining Buffer | BioLegend | Cat#420201 |
| Simvastatin | Thermo Fisher | Cat#PHR1438 |
| A-922500 | Sigma Aldrich | Cat#A1737 |
| PF-06424439 | Sigma Aldrich | Cat#PZ0233 |
| C75 | Abcam | Cat#ab141397 |
| YTX-465 | MedChemExpress | Cat#HY-124751 |
| GSK2033 | Cayman Chemical | Cat#CAY25443 |
| SPiDER-βGal | Dojindo | Cat#SG02-10 |
| Chloroquine | Sigma Aldrich | Cat#C6628-25G |
| **Critical commercial assays** | | |
| High-Capacity cDNA Reverse Transcription Kit | Thermo Fisher | Cat#4368813 |
| TaqMan Fast Universal PCR Master Mix | Thermo Fisher | Cat#4352042 |
| Pierce BCA Protein Assay kit | Thermo Fisher | Cat#23227 |
| RNeasy Mini Kit | Qiagen | Cat#74106 |
| DNeasy Blood & Tissue Kit | Qiagen | Cat#69506 |
| CytoTune-iPS 2.0 Sendai Reprogramming Kit | Thermo Fisher | Cat#A16517 |
| StemRNA Reprogramming Kit | REPROCELL | Cat#00-0076 |
| Seahorse XF Cell Mito Stress Test Kit | Agilent | Cat#103015-100 |
| CellTox Green Cytotoxicity Assay | Promega | Cat#G8742 |
| **Deposited data** | | |
| Proteomics | MassIVE | MSV000095283 |
| Intracellular metabolomics | Metabolomics Workbench | Study ID: ST003331 |
| Extracellular metabolomics | Metabolomics Workbench | Study ID: ST003332 |
| Intracellular lipidomics | Metabolomics Workbench | Study ID: ST003328 |
| Extracellular lipidomics | Metabolomics Workbench | Study ID: ST003330 |
| **Experimental models: Cell lines** | | |
| Fibroblasts | This study and Douvaras et al.[84] | See also Table S1 |
| WIBJ iPSCs | Cambridge BioResource | Gift from Dr. Alessandra Granada; See also Table S1 |
| SH-SY5Y | ATCC | CRL-226; (Gift from Michael Whitehead) |
| **Oligonucleotides** | | |
| FAM-MGB Taqman Gene expression Assay CDKN1A | Thermo Fisher | Cat#4331182; Assay ID:Hs00355782_m1 |
| FAM-MGB Taqman Gene expression Assay CDKN2A | Thermo Fisher | Cat#4331182; Assay ID:Hs00923894_m1 |
| FAM-MGB Taqman Gene expression Assay TP53 | Thermo Fisher | Cat#4331182; Assay ID:Hs01034249_m1 |
| FAM-MGB Taqman Gene expression Assay APOE | Thermo Fisher | Cat#4331182; Assay ID:Hs00171168_m1 |
| FAM-MGB Taqman Gene expression Assay ABCA1 | Thermo Fisher | Cat#4331182; Assay ID:Hs01059101_m1 |
| VIC 18s rRNA Control Mix | Thermo Fisher | Cat#4318839 |
| FAM-MGB Taqman Gene expression Assay MT-ND2 | Thermo Fisher | Cat#4331182; Assay ID:Hs02596874_g1 |
| VIC Number Reference Assay RNaseP | Thermo Fisher | Cat#4401631 |
| Custom primers | Thermo Fisher | Custom-manufactured (Table S2) |
| **Software and algorithms** | | |
| Adobe Illustrator | Adobe | N/A |
| Fiji | GNU General Public License | N/A |

(*Continued on next page*)

*Continued*

| REAGENT or RESOURCE | SOURCE | IDENTIFIER |
|---|---|---|
| Prism | GraphPad | N/A |
| Seahorse Wave Desktop | Agilent | N/A |
| FlowJo | BD | N/A |
| Metaboanalyst | Wishart Research Group, University of Alberta | https://www.metaboanalyst.ca/ |
| BioPAN | Gaud et al.[43] | https://www.lipidmaps.org/biopan/ |
| LINEX$^2$ | Rose et al.[42] | https://exbio.wzw.tum.de/linex/ |
| bulkAnalyseR | Moutsopoulos et al.[89] | https://github.com/Core-Bioinformatics/bulkAnalyseR |
| MOFA | Argelaguet et al.[60] | https://biofam.github.io/MOFA2/ |
| GENIE3 | Huynh-Thu et al.[92] | https://bioconductor.org/packages/release/bioc/html/GENIE3.html |
| Gprofiler2 | Raudvere et al.[91] | https://CRAN.R-project.org/package=gprofiler2 |
| edgeR | Robinson et al.[90] | https://bioconductor.org/packages/release/bioc/html/edgeR.html |
| MOFA and Covariation Network Code | This study | https://doi.org/10.5281/zenodo.13764808 |

## EXPERIMENTAL MODEL AND SUBJECT DETAILS

The cohort consists of 4 PMS (3 SPMS and 1 PPMS) and 3 healthy control donors between 25 and 63 years of age. The cohort includes representation from both genders (5 male and 2 female), evenly distributed across PMS and control groups (Table S1). PMS donors underwent clinical assessment when recruited for the study. Fibroblasts were provided by the New York Stem Cell Foundation (NYSCF) Research Institute through their Repository (http://www.nyscf.org/repository).[83] Patients were recruited at the Tisch Multiple Sclerosis Research Center of New York, upon informed consent and institutional review board approval (BRANY). Control fibroblasts from lines A and B (Table S1) were generated from adult dermal fibroblasts after obtaining consent and ethical clearance by the ethics committee of the University of Würzburg, Germany. All other fibroblasts used in this study were obtained from NYSCF.

### Derivation and reprogramming of skin fibroblasts to iPSCs and iNSCs

Derivation and reprogramming of skin fibroblasts to iPSCs was performed as previously described for the NYSCF cohort.[84] Briefly, 3-5 mm skin biopsies were collected in Biopsy Collection Medium (RPMI 1460 [Thermo Fisher] with 1X Antibiotic-Antimycotic [Thermo Fisher]), cut into smaller pieces (<1 mm) and plated onto a TC-treated 35 mm dish in Biopsy Plating Medium, composed by Knockout DMEM (Thermo Fisher), 2 mM GlutaMax (Thermo Fisher), 0.1 mM non-essential amino acids (Thermo Fisher), 0.1 mM β-Mercaptoethanol (Thermo Fisher), 10% Fetal Bovine Serum (FBS) (Thermo Fisher), 1X Penicillin-Streptomycin (P/S) (Thermo Fisher) and 1% Nucleosides (Millipore). Once the first fibroblasts migrated out of the biopsies, the cultures were maintained in growth medium (DMEM Glutamax I [Thermo Fisher] supplemented with 10% fetal bovine serum, 1% non-essential amino acids and 1 mM sodium pyruvate (Thermo Fisher) at 37°C with 5 % $CO_2$ and fed every 3-4 days. After reaching 90% confluency the fibroblasts were detached with trypsin-EDTA 0.05% for 5 min followed by neutralization in DMEM and spun down at 300xg for 5 min. They were split 1:4 into growth media.

Fibroblasts at passage 3-5 were reprogrammed to iPSCs using the integration free technology based on non-modified RNA plus microRNA (kit from REPROCELL, formerly Stemgent), following manufacturer's instructions. About 25x10$^3$ fibroblasts/well were plated onto Matrigel-coated 12-well plates in culture medium for 24 hours and then in NuFF-conditioned Pluriton reprogramming medium with B18R. Cells were transfected for 11 consecutive days using Stemfect as following: day 0 microRNA only, days 1-3 RNA only, day 4 microRNA plus RNA, days 5-11 RNA only. From day 11, TRA-1-60$^+$ colonies (live stained) were manually picked and replated on mouse embryonic fibroblasts in HUESM medium (Knockout-DMEM, 20% knock-out serum, glutamax 2mM, NEAA 0.1mM, 1X P/S and β-mercaptoethanol 0.1mM [Thermo Fisher]). Pluripotent colonies were passaged and adapted to feeder-free conditions with hESC matrigel (Corning) and mTeSR1 (STEMCELL Technologies) medium. The WIBJ iPSC line, obtained from Cambridge BioResource as a gift from Alessandra Granada, was reprogrammed from fibroblasts using the CytoTune 1 non-integrating kit (Thermo Fisher). iPSC media was changed every day. When confluent, cells were lifted using accutase (Thermo Fisher), spun at 300xg for 5 min, and split 1:10-1:20 onto hESC-matrigel coated plates with Y-27632 (10 uM) (Thermo Fisher) in mTeSR1 media.

To generate directly induced neural stem cells (iNSCs) from fibroblasts we used a nonintegrating Sendai virus-based direct conversion strategy, as previously described.[32] Briefly, fibroblasts were seeded at 75,000/well in fibroblast media in a non-coated

12-well. On the next day the fibroblasts were transduced using the CytoTune-iPS 2.0 Sendai Reprogramming Kit (Thermo Fisher) with hKOS (MOI: 3), hc-Myc (MOI: 3), hKlf4 (MOI: 3). The day following transfection, the medium was switched to neural induction medium (NIM) [DMEM:F12 and Neurobasal (1:1), supplemented with N2 supplement (1x, Thermo Fisher), 1% glutamax, B27 supplement (1x, Thermo Fisher), CHIR99021 (3 μM, Cell Guidance Systems), SB-431542 (2 μM, Cayman Chemicals) and hLIF (10 ng/ml, Cell Signaling Technology)], and cells were moved to 39°C with 5% $CO_2$ to achieve viral clearance over 14 days. A few samples were collected here to generate positive controls for quality control assays. Medium changes were performed every other day. Following 25 days of transfection, iNSC colonies were manually selected, seeded onto Growth Factor Reduced (GFR) Matrigel Matrix (1:20 in DMEM/F12) coated plates for expansion, and subjected to quality control assays. iNSCs were maintained in NIM media until 70% confluent, then lifted using accutase (Thermo Fisher), spun at 300xg for 5 mins, and plated onto GFR-Matrigel coated plates with Y-27632 (10 μM, Miltenyi Biotec) between 1:3-1:5 in NIM media. Media was changed every second day as needed. Experiments were performed on cells from passages 20-40.

## METHOD DETAILS

### Trilineage Differentiation

Trilineage differentiation of the iPSCs was achieved using the STEMdiff Trilineage Differentiation Kit (STEMCELL Technologies). Media were prepared based on kit instructions. For ectodermal differentiation iPSCs were plated at 200,000 cells/$cm^2$, mesoderm at 50,000 cells/$cm^2$, and endoderm 200,000 cells/$cm^2$. Mesoderm and endodermal differentiations were fed with indicated media every day for 5 days, then collected for RNA isolation or fixed for immunocytochemistry. Ectodermal differentiations were fed every day for 7 days then collected.

### RNA Isolation, RT-PCR, and qRT-PCR

Total RNA from all cell types was isolated using the RNeasy Mini Kit (Qiagen) following manufacturer's instructions. Briefly, cells were washed with ice-cold PBS followed by the addition of RLT lysis buffer. Samples were then stored at -80°C until extraction. Total RNA was then quantified with the NanoDrop 2000c instrument (Thermo Fisher).

iNSC quality control was performed using RT-PCR analysis. Here 300 ng of RNA was reverse-transcribed using the High Capacity cDNA Reverse Transcription Kit (Thermo Fisher) according to the manufacturer's instructions using a 20 μL reaction volume on a T100 Thermal Cycler (BioRad, 1861096). The RT-PCR reaction was made using DreamTaq buffer (Thermo Fisher), dNTPs (2 mM each, Thermo Fisher), forward and reverse primers (0.5 μM, Table S2), DreamTaq Hot Start DNA Polymerase (Thermo Fisher), and finished to 24 μL with water. 1 μL of cDNA from each sample was loaded into the PCR reaction. *OCT4* reactions were cycled at: 95°C for 3 mins; x30 cycles of 95°C 30 sec, 60°C 30 sec, 72°C 1 min; 72°C 5 min, hold at 4°C. *SeV*, *KOS*, *c-Myc*, *SOX2*, *PAX6*, and *NES* reactions were cycled at: 95°C for 3 mins; x30 cycles of 95°C 30 sec, 55°C 30 sec, 72°C 1 min; 72°C 5 min, hold at 4°C. Samples were diluted with Gel Loading Dye (New England BioLabs), and 5 μL was loaded into a 2% agarose gel (Thermo Fisher) in 1X TAE buffer (MP Biomedicals). TrackIt 100 bp DNA Ladder (Thermo Fisher) was used to assess band size. DNA was visualized using Gelred Stain (Biotium) in the gel and imaged on a BioRad XR GelDoc Imager.

For qRT-PCR analysis, 500 ng of RNA was reverse-transcribed using the High Capacity cDNA Reverse Transcription Kit (Thermo Fisher) according to the manufacturer's instructions using a 20 μL reaction volume on a T100 Thermal Cycler (BioRad). qRT-PCR was performed with the TaqMan Fast Universal PCR Master Mix (2x) (Thermo Fisher) and TaqMan Gene Expression Assays (see key resources table). Ribosomal subunit 18S was used to normalize gene expression. 1.5 μL of cDNA from each sample was run in duplicate using a QuantStudio 7 Flex (Thermo Fisher) and analyzed with the $2^{-\Delta\Delta CT}$ method.

### Immunocytochemistry for iNSCs, iPSCs, and Trilineage Differentiation

Cells were plated at a density between 40,000 – 60,000 cells/$cm^2$ on GFR-matrigel coated glass coverslips. Cells were fixed for 10 minutes with 4% paraformaldehyde (Thermo Fisher) then permeabilized for 10 minutes in PBS with 0.25% Triton-X100 (Thermo Fisher). Cells were then blocked for 1 hour using 1% normal donkey serum (Thermo Fisher) in PBS with 0.1% Triton-X100. Cells were incubated with the following primary antibodies in the above blocking buffer: Nestin (Novus Biolgicals, 1:500), ETNPPL (Atlas, 1:500), SOX2 (Abcam, 1:500), SSEA4 (Thermo Fisher, 1:100), Nanog (Abcam, 1:1000), Oct4 (Santa Cruz, 1:200), SOX17 (R&D, 1:200), ACTA2 (antibodies.com, 1:20), Pax6 (BioLegend, 1:100), SOX1 (R&D, 1:50), OCT4 (Reprocell, 1:250), TRA-1-60 (EMD Millipore, 1:250), TRA-1-81 (EMD Millipore, 1:250), NANOG (Cell Signaling, 1:100), SSEA4 (Abcam, 1:250), and SOX2 (Reprocell, 1:250) at 4°C overnight. Coverslips were washed three times for 10 minutes each in PBS with 0.1% Triton-X100 then incubated with species appropriate secondary antibodies (1:1000) in blocking buffer for one hour at room temperature. Coverslips were washed again as above then stained with DAPI in PBS (300 nM, Thermo Fisher) for five minutes then washed in PBS. Coverslips were mounted onto glass slides using Fluoromount-G (Thermo Fisher). Images were taken on a Leica DMI400B microscope at 40X in oil immersion.

### SPiDER-β Galactosidase Detection by Flow Cytometry

iNSCs were plated at 300,000 cells/well in GFR-matrigel coated 12-well plates in triplicate. For assessment of senescence after simvastatin treatment, cells were treated with the vehicle or simvastatin (10 μM) 24 hours after plating. 72 hours after plating, cells were treated with choloroquine (Sigma-Aldrich) at a concentration of 150 μM for 1 hour at 37°C to inhibit endogenous β-galactosidase activity. The cells were next washed with iNSC media once and then treated with SPiDER-βgal (1:1000, Dojindo) in iNSC media

and incubated at 37°C. After 30 minutes the cells were washed once with PBS, lifted using accutase, and pelleted at 300xg for 5 mins. Cells were resuspended in cell staining solution. Before analysis SYTOX Blue (Thermo Fisher) was added to the sample. Cells were analysed by flow cytometry on a CytoFlex Flow Cytometer (Beckman Coulter), recording 100,000 total events. Analysis was performed using FlowJo v10 (BD Biosciences). First, debris was removed by gating cells using SSC-H by FSC-H, next a single cell population was gated using FSC-H by FSC-A, next live cells were gated using the SYTOX Blue negative population. SPiDER-βgal fluorescence intensity was assessed on the PE laser and SYTOX Blue on the PB450 laser.

### Immunoblotting

Cells were homogenized in 1x RIPA buffer (Abcam) supplemented with 1x protease and phosphatase inhibitors (Thermo Fisher). Equal protein amounts (10 μg) were resolved by SDS-PAGE on 4-15% Mini-PROTEAN TGX Stain Free gels (30 μL, 10 well comb, BioRad) and transferred to polyvinylidene fluoride (PVDF) membranes using a Trans-Blot Turbo Transfer Pack (BioRad). Membranes were blocked with 5% milk in 0.1% TBST for one hour at room temperature. Membranes were then immunoblotted over night at 4°C with the indicated primary antibodies diluted in blocking buffer: Phosphorylated Stat1 (Tyr701) (D4A7) (Cell Signaling, 1:1000), STAT1 (Cell Signaling, 1:1000), ISG15 (Cell Signaling, 1:1000), β-actin (Thermo Fisher, 1:5000). Membranes were washed three times with TBST for 5 minutes and immunoblotted with the appropriate HRP-conjugated secondary antibodies: anti-rabbit (Cell Signaling, 1:2000) or anti-mouse (Cell Signaling, 1:2000). Membranes were washed three times with TBST for 5 minutes, then imaged on a ChemiDoc MP Imaging System (BioRad), soaked in Clarity Western ECL Substrate (BioRad). Protein band densitometry was measured in ImageJ. An identical selection frame was used to determine the mean gray value (MGV) measurement of protein bands and background areas above and below each band. Band intensity (BI) was determined by the formula: $BI = (255\text{-}MGV_{protein\ band}) - [(255 - MGV_{background\ above}) + (255 - MGV_{background\ below})]/2$. BI values for PMS iNSC lines were normalized to the BI values of control iNSC lines within each blot.

### Immunocytochemistry for mitochondrial morphology assay

Cell lines were plated in technical triplicates at a density between 40,000 – 60,000 cells/cm$^2$ on GFR-matrigel coated glass coverslips. Cells were fixed for 10 minutes with 4% paraformaldehyde then washed twice with PBS for 5 minutes. Cells were then blocked for 1 hour using 1% normal goat serum in PBS with 0.1% Triton-X100. Cells were incubated with TOMM20 (Abcam, 1:1000) at 4°C overnight in the above blocking buffer. Coverslips were washed again as above then stained with DAPI in PBS (300 nM) for five minutes then washed in PBS. Coverslips were mounted onto glass slides using Fluoromount-G. 4 regions of interest (ROIs) were imaged on each coverslip, acquiring 36 Z-stacks with a step size of 0.2 μm on a Leica SPE Confocal microscope at 63X in oil immersion and analyzed using Fiji. Maximal projection images of each ROI were generated for the TOMM20 channel, and 48 random single-cell selections were made (4 cells/ROI, 3 ROIs/coverslip, 3 coverslips/cell line). The resulting single-cell selections were analyzed using the MiNA plugin.[85] MiNA estimates mitochondrial footprint from a binarized copy of the image as well as the lengths of mitochondrial structures using a topological skeleton.

### Seahorse mitochondrial stress test

A Seahorse calibration plate was rehydrated with XF calibration solution (Agilent) overnight in a non-$CO_2$ incubator at 37°C. On the same day, fibroblasts were seeded at 45 x 10$^3$ cells per well (5-10 replicates per cell line) in fibroblast growth media in a Seahorse XFe24 Microplate (Agilent, 100777-004) and incubated for 24 hours to allow cells to adhere. Similarly, iNSCs were seeded at 12 X 10$^4$ cells per well (5-10 replicates per cell line) in NIM media in a Seahorse XFe24 Microplate coated with GFR-matrigel and incubated for 24 hours to allow cells to adhere. To assess activity after simvastatin treatment, iNSCs were plated as described above and after 24 hours cells were treated with vehicle or simvastatin (10 μM) supplemented NIM for 48 hours. In each microplate 4 wells were left empty to serve as background wells, as per manufacturer's protocol guidelines. The calibration plate was then calibrated using the Seahorse instrument. For measurements of iNSCs without treatment, the cells were washed once with DMEM Assay Medium (XF DMEM [Agilent] supplemented with XF glucose [10 mM, Agilent], XF glutamine [2 mM, Agilent] and XF pyruvate [1 mM, Agilent]), then left in DMEM Assay Medium and placed in a non-$CO_2$ incubator for 1 hour. Cells were then subjected to the XFe Cell Mito stress test (Agilent) on a Seahorse XFe24 Analyzer (Agilent) according to the manufacturer's instructions. The cell plate was equilibrated, and the baseline was measured. Oligomycin was used to inhibit mitochondrial ATP production (2 μM final concentration in well). FCCP was used to induce mitochondrial uncoupling and maximal mitochondrial respiration (2 μM final concentration in well). Rotenone/antimycin A (Rot/AA) were used to inhibit mitochondrial complex I and complex III respectively, and therefore stop mitochondrial respiration (1 μM final concentration in well). Three reads were obtained (every 8.75 minutes) at baseline and after each drug injection. For only the PMS vehicle or simvastatin treated Seahorse plate, the cells were fed with XF DMEM (Agilent) media without glucose, glutamine, and pyruvate supplements for 1 hour in a non-$CO_2$ incubator to deplete the glycolytic pathway. Cells were then subjected to the XFe Cell Mito stress test (Agilent). First, glucose was given to the cells (10 mM final concentration in the well), then oligomycin, FCCP, and rotenone/antimycin A as described above. If cells did not respond to the addition of drugs, they were excluded from further analysis. After the mitochondrial stress test on fibroblasts protein levels of each well were measured from the cell lysates by Pierce BCA Protein Assay and used for signal normalization. Due to the use of extracellular matrix coating for iNSC culturing, normalization by nuclear count was performed. After the mitochondrial stress test iNSC plates were fixed with 4% paraformaldehyde, stained with DAPI and 9 ROIs were captured per well at 10X magnification on a Leica DMI400B microscope.

Nuclear counts were determined using the Threshold, Watershed, and Analyze particles functions in Fiji and used for signal normalization. Analysis was performed using the Wave 2.6.1. software (Agilent).

### Cell size, mitochondrial mass, and membrane potential

iNSCs were plated in technical duplicate, in two separate experiments, at a density of 800,000 cells/well on GFR-matrigel coated 6-well plates. Cells were lifted with accutase, spun for 5 minutes at 300 x g and washed once with 1x staining buffer (BioLegend). iNSCs were stained in suspension for 15 minutes at 37°C on an orbital shaker (500 rpm), with 100 nM of the mitochondrial mass indicator MitoTracker Green (Invitrogen), 50 mM of the mitochondrial membrane potential indicator (MitoTracker Red CMXRos FM) and 1x of the live/dead stain Zombie Violet diluted in staining buffer. Cells were washed once with staining buffer and analyzed by flow cytometry on a BD LSRFortessa Flow Cytometer (BD Biosciences), recording 100,000 total events. Analysis was performed using FlowJo v10 (BD Biosciences). First a single cell population was gated using FSC-H by FSC-A, next live cells were gated using the ZombieViolet negative population. The mean cell size of iNSCs was estimated from the geometric mean of the forward-scatter area (FSC-A) parameter in the gated population. Histograms of red (mitochondrial membrane potential) and green (mitochondrial mass) fluorescence were assessed, and geometric means (i.e., mean fluorescence intensities) were extracted. The mitochondrial mass signal was used for normalization of the mitochondrial membrane potential signal. Resulting values for PMS iNSCs were further normalized to control levels set to a value of 1.

### Mitochondrial superoxide levels

iNSCs were plated in technical duplicate, in two separate experiments, at a density 800,000 cells/well on GFR-matrigel coated 6-well plates. Cells were lifted with accutase, spun for 5 minutes at 300 x g and washed once with 1x staining buffer (BioLegend). iNSCs were stained in suspension for 30 minutes at 37°C on an orbital shaker (500 rpm), using 5 μM of the mitochondrial superoxide indicator MitoSox (Invitrogen) and 1x of the live/dead stain Zombie Violet diluted in staining buffer. Cells were washed once with staining buffer and analyzed by flow cytometry on a BD LSRFortessa Flow Cytometer (BD Biosciences), recording 100,000 total events. Analysis was performed using FlowJo v10 (BD Biosciences). First a single-cell population was gated using FSC-H by FSC-A, next live cells were gating using the ZombieViolet negative population. The histogram of red fluorescence was assessed, and the geometric mean (i.e., mean fluorescence intensity) was extracted. Resulting values for PMS iNSCs were further normalized to control levels set to a value of 1.

### Mitochondrial copy number assay

Total DNA from all cell types was isolated using the DNeasy Blood & Tissue Kit (Qiagen) according to manufacturer's instructions. Total DNA was then quantified with the NanoDrop 2000c instrument (Thermo Fisher). For each sample, 20 ng of DNA was loaded into a qPCR reaction containing the indicated primers for MT-ND2 and the TaqMan Fast Universal PCR Master Mix (Thermo Fisher) and ran on a QuantStudio 7 Flex (Thermo Fisher). The RNase P TaqMan Copy Number Reference Assay was used for normalization within the same sample, using the with the $2^{-\Delta\Delta CT}$ method.

### Simvastatin activation

Simvastatin requires activation through the opening of the lactone ring before it can be used in cell culture. To achieve this, we followed the procedure outlined by Merck. In summary, 8 mg of simvastatin was dissolved (0.019 mM) in 0.2 mL of 100% ethanol. Subsequently, 0.3 mL of 0.1 N NaOH was added to the solution. The mixture was then heated at 50°C for 2 hours and later adjusted to a pH of 7.2 with HCl. The resulting solution was adjusted to a final volume of 1 mL using distilled water, aliquoted and stored at -80 °C until used to supplement cell culture media.

### Cytotoxicity Assay

The cytotoxicity of simvastatin (Thermo Fisher, 1-100 μM), A-922500 (Sigma Aldrich, 0.1-10 μM) and PF-06424439 (Sigma Aldrich, 1-100 μM), C75 (Abcam, 1-100 μM), GSK2003 (Cayman Chemical, 5.2-520 nM), and YTX-465 (MedChemExpress, 3-300 μM) on iNSCs was measured using the CellTox Green Cytotoxicity Assay (Promega) according to the manufacturer's instructions. Control and PMS iNSCs were seeded at 25,000 cells per well on GFR-matrigel-coated black 96-well clear-bottom plates (Thermo Fisher) in iNSC media. 24 hours after plating the iNSCs were treated with varying doses of the above drugs in iNSC media. 48 hours after treatment, the medium was removed, and the cells were incubated with Hoechst (1 ug/mL) at room temperature for 10 minutes followed by fluorescent measurement at 358 nm excitation and 461 nm emission on a Tecan Infinite M200 Pro plate reader. Next, the cell lysis solution, provided with the assay, was added to the designated wells for 30 minutes at room temperature as a positive cell death control. The cells were next incubated with the CellTox reagent for 15 minutes at room temperature. The fluorescence was then measured at 485-500 nm excitation and 520-530 emission. Toxicity was measured by subtracting medium-only background fluorescence from the Hoechst and CellTox stains, and the ratio of the CellTox over Hoechst fluorescence for each well was calculated. This was then normalized to vehicle control measurements.

### Immunocytochemistry for lipid droplet quantification

iNSCs were plated in technical triplicates at a density between 40,000 – 60,000 cells/cm$^2$ on GFR-matrigel coated 13 mm diameter glass coverslips. Fibroblasts were plated in technical triplicates at a density between 25,000 – 37,500 cells/cm$^2$ on GFR-matrigel

coated 13 mm diameter glass coverslips. Cells were then collected after 72 hours. For drug treatments, iNSCs were plated at 100,000 cells per well in iNSC media. After 24 hours the media was replaced with fresh media with varying drugs (1 μM A-922500 and 10 μM PF-06424439, 10 μM C75, 52 nM GSK2003, 30 μM YTX-465). After 48 hours the cells were collected. Cells were fixed for 10 minutes with 4% paraformaldehyde then washed twice with PBS for 5 minutes. LDs were stained using the 1x LipidSpot610 dye for 20 minutes at room temperature. Coverslips were then counter stained with DAPI in PBS (300 nM) for five minutes then washed in PBS and mounted onto glass slides using Fluoromount-G (Thermo Fisher). 4 ROIs were imaged on each coverslip using a Leica DMI400B microscope at 63X in oil immersion and batch analyzed using Fiji. LD numbers and nuclei numbers were measured using the Threshold, Watershed, and Analyze particles functions in Fiji, and LD content was calculated as a ratio of LD count/nuclei count.

### High resolution imaging and 3D reconstruction of lipid droplets

Cell lines were plated at a density between 40,000 – 60,000 cells/cm$^2$ on GFR-matrigel coated 8-well glass chamber slides. Cells were fixed for 10 minutes with 4% paraformaldehyde. Plasma membrane was stained using BioTracker 555 Orange Cytoplasmic Membrane Dye (1:1000) and LDs were stained with 1x LipidSpot™ in PBS for 20 minutes at room temperature. Nuclei were stained with 300 nM DAPI in 1x PBS. Cells were then washed with 1x PBS twice for 5 minutes. Z-stack Lightning imaging with a 0.2 μm step size was performed using confocal microscope Leica Stellaris8 on a 63x objective and oil immersion setting. 3D surfaces for each staining where then rendered using the Imaris 9.5 software.

### Sample generation for metabolomics, stable isotope tracing, proteomics, and lipidomics

iNSCs were seeded in NIM with Y-27632 (10 μM) at a density of 100,000 cells/cm$^2$ GFR-matrigel coated wells, in technical triplicates per line. Medium was changed the next day. Glucose tracer experiments were run on day 2 after seeding by removing the culture medium and adding glucose-free NIM [DMEM:F12 w/o glucose and Neurobasal (1:1), supplemented with N2 supplement (1x, Thermo Fisher), Glutamax (Thermo Fisher, 3.2 mM), pyruvate (Agilent, 0.35 mM), B27 supplement (1x, Thermo Fisher), CHIR99021 (3 μM, Cell Guidance Systems), SB-431542 (2 μM, Cayman Chemicals) and hLIF (10 ng/ml, Cell Signaling Technology)] supplemented with D-Glucose-$^{13}C_6$ (Thermo Fisher, 20.4 mM). Samples were collected after 30 minutes (for optimal resolution of glycolysis), 6 hours (for assessment of protein acetylation) and 24 hours (for optimal resolution into TCA cycle and anabolic metabolic pathways). The glutamine tracer experiment was run on day 2 after seeding by removing the culture medium and adding glutamine-free NIM [DMEM:F12 w/o glutamine and Neurobasal (1:1), supplemented with N2 supplement (1x, Thermo Fisher), glucose (Agilent, 20.4 mM), pyruvate (Agilent, 0.35 mM), B27 supplement (1x, Thermo Fisher), CHIR99021 (3 μM, Cell Guidance Systems), SB-431542 (2 μM, Cayman Chemicals) and hLIF (10 ng/ml, Cell Signaling Technology)] supplemented with L-Glutamine-$^{13}C_5$,$^{15}N_2$ (Thermo Fisher, 3.2 mM). Samples were collected after 24 hours (for optimal resolution into TCA cycle and anabolic metabolic pathways). For intracellular lipidomics analysis, medium was changed 24 hours after seeding to vehicle- or SV-supplemented NIM, and cells were further incubated for 48 hours. Samples were collected on day 3 after seeding (no other medium changes were done except for the day 1 feeding with fresh NIM supplemented with vehicle or SV). Samples for extracellular lipidomics analysis were collected on day 3 after seeding, concurrently with 24 hours glucose tracing experiments. Sample collection was performed on ice. Conditioned culture medium was collected, spun at 300 x g for 5 minutes to remove cellular debris and 100 μL was stored at -80°C until sample processing. Cells were then lifted using accutase and spun at 300 x g for 5 mins. Cell pellets were resuspended in PBS for counting and spun once more at 300 x g for 5 mins. Supernatants were aspirated and cell pellets were stored at -80°C until sample processing. Mass spectrometry-based omics analyses were performed on frozen cell pellets at the University of Colorado School of Medicine Mass Spectrometry Facility, a shared resource of the University of Colorado Cancer Center.

### Sample processing for metabolomics and stable isotope tracing

Metabolites from frozen pellets were extracted at 2e6 cells per mL using ice cold 5:3:2 methanol:acetonitrile:water (v/v/v) with vigorous vortexing at 4°C followed by centrifugation as described. Clarified supernatants were analyzed (10 μL per injection) by ultra-high-pressure liquid chromatography coupled to mass spectrometry on a Vanquish UHPLC (Thermo Fisher) coupled to a Q Exactive mass spectrometer (Thermo Fisher) in positive and negative ion modes (separate runs). The UHPLC utilized a 5 min C18 gradient at 450 μL/min; eluate was introduced to the MS via electrospray ionization as previously described in detail.[86] Data analysis and quality control measures were performed as described.[86,87] Isotopologue data from stable isotope tracing experiments was corrected for natural abundance then plotted using GraphPad Prism 10.0.

### Sample processing for proteomics analysis

The protein pellets after metabolomics extraction were solubilized in 4% SDS in 100 mM triethylammonium bicarbonate (TEAB) pH 7.0 lysis buffer. The samples were digested in the S-Trap micro spin column (Protifi, Huntington, NY) following the manufacturer's procedure. Samples were reduced with 10 mM DTT at 55°C for 30 min, cooled to room temperature, and then alkylated with 25 mM iodoacetamide in the dark for 30 min. Next, a final concentration of 1.2% phosphoric acid and then six volumes of binding buffer (90% methanol; 100 mM triethylammonium bicarbonate, TEAB; pH 7.0) were added to each sample. After gentle mixing, the protein solution was loaded to a S-Trap micro spin column, spun at 1500 x g for 2 min, and the flow-through collected and reloaded onto the S-Trap micro spin column. This step was repeated three times, and then the S-Trap micro spin column was washed with 400 μL of binding buffer 3 times. Finally, 1 μg of sequencing-grade trypsin (Promega) and 125 μL of digestion buffer (50 mM TEAB) were added onto the filter and digested carried out at 37 °C for 6 hours. To elute peptides, three stepwise buffers were applied,

with 100 μL of each with one more repeat, including 50 mM TEAB, 0.2% formic acid in water, 50% acetonitrile, and 0.2% formic acid in water. The peptide solutions were pooled, lyophilized, and resuspended in 100 μl of 0.1% FA.

Conditioned media samples were digested according to the FASP protocol using a 10 kDa molecular weight cutoff filter. In brief, samples were mixed in the filter unit with 8 M urea, 0.1 M ammonium bicarbonate (AB) pH 8.0, and centrifuged at 14,000 g for 15 min. The proteins were reduced with 10 mM DTT for 30 min at RT, centrifuged, and alkylated with 55 mM iodoacetamide for 30 min at RT in the dark. Following centrifugation, samples were washed 3× with 8 M urea, and 3× with 50 mM AB, pH 8.0. Protein digestion was carried out with sequencing grade modified trypsin (Promega) at 1/50 protease/protein (wt/wt) at 37°C overnight. Peptides were recovered from the filter using 50 mM AB. Samples were dried via Speed-Vac and desalted and concentrated on Thermo Scientific Pierce C18 Tip.

### Proteomics data acquisition

A 20 μL volume of each sample was loaded onto individual Evotips for desalting and then washed with 20 μL 0.1% FA followed by the addition of 100 μL storage solvent (0.1% FA) to keep the Evotips wet until analysis. The Evosep One system (Evosep, Odense, Denmark) was used to separate peptides on a Pepsep column, (150 um inter diameter, 15 cm) packed with ReproSil C18 1.9 μm, 120 A resin. The system was coupled to the timsTOF Pro mass spectrometer (Bruker Daltonics, Bremen, Germany) via the nano-electrospray ion source (Captive Spray, Bruker Daltonics).

The mass spectrometer was operated in PASEF mode. The ramp time was set to 100 ms and 10 PASEF MS/MS scans per topN acquisition cycle were acquired. MS and MS/MS spectra were recorded from m/z 100 to 1700. The ion mobility was scanned from 0.7 to 1.50 Vs/cm$^2$. Precursors for data-dependent acquisition were isolated within ± 1 Th and fragmented with an ion mobility-dependent collision energy, which was linearly increased from 20 to 59 eV in positive mode. Low-abundance precursor ions with an intensity above a threshold of 500 counts but below a target value of 20000 counts were repeatedly scheduled and otherwise dynamically excluded for 0.4 min.

### Proteomics Database Searching and Protein Identification - *Cells*

MS/MS spectra were extracted from raw data files and converted into.mgf files using MS Convert (ProteoWizard, Ver. 3.0). Peptide spectral matching was performed with Mascot (ver. 2.5) against the Uniprot human database. Mass tolerances were +/- 15 ppm for parent ions, and +/- 0.4 Da for fragment ions. Trypsin specificity was used, allowing for 1 missed cleavage. Met oxidation, protein N-terminal acetylation, Lys C13 acetylation and peptide N-terminal pyroglutamic acid formation were set as variable modifications with Cys carbamidomethylation set as a fixed modification.

Scaffold (version 5.0, Proteome Software, Portland, OR, USA) was used to validate MS/MS based peptide and protein identifications. Peptide identifications were accepted if they could be established at greater than 95.0% probability as specified by the Peptide Prophet algorithm. Protein identifications were accepted if they could be established at greater than 99.0% probability and contained at least two identified unique peptides.

### Database Searching and Protein Identification – *Conditioned media*

Raw data files conversion to peak lists in the MGF format, downstream identification, validation, filtering, and quantification were managed using FragPipe version 13.0. MSFragger version 3.0 was used for database searches against a mouse database with decoys and common contaminants added. The identification settings were as follows: Trypsin, Specific, with a maximum of 2 missed cleavages, up to 2 isotope errors in precursor selection allowed for, 10.0 ppm as MS$^1$ and 20.0 ppm as MS$^2$ tolerances; fixed modifications: Carbamidomethylation of C (+57.021464 Da), variable modifications: Oxidation of M (+15.994915 Da), hydroxylation of P (+15.994915 Da), acetylation of protein N-term (+42.010565 Da), pyrolidone from peptide N-term Q or C (-17.026549 Da).

### Protein acetylation

The $^{13}$C acetylated peptides were identified using the Mascot search algorithm by searching all MS/MS spectra against the human database for [$^{13}C_2$]lysine as a variable modification. The quantitative MS analysis of the $^{13}$C acetylation sites were performed based on the spectral count data (i.e. peptide spectral matches).

### Lipidomics sample processing

Lipids were extracted from frozen cells at 2e6 cells/mL and from conditioned media at 1:25 dilution with cold MeOH. Suspensions were briefly vortexed and placed at -20°C for 30 min followed by a vigorous vortex for 30 min at 4°C. Insoluble material was pelleted by centrifugation (18,213 x g, 10 min, 4 °C) and supernatants were isolated for analysis. Lipidomics analysis employed a Thermo Vanquish UHPLC system coupled to a Thermo Q Exactive mass spectrometer. 5 uL injections of the samples were resolved across a 2.1 x 30 mm, 1.7 μm Kinetex C18 column (Phenomenex) using a 5-minute, reverse-phase gradient adapted from a previous method. The Q Exactive was run independently in positive and negative ion mode, scanning using full MS from 125-1500 m/z at 70,000 resolution and top 10 data-dependent MS$^2$ at 17,500 resolution. Electrospray ionization was achieved with 45 Arb sheath gas, 25 Arb auxiliary gas, and 4 kV spray voltage. Calibration was performed prior to the run using the PierceTM Positive and Negative Ion Calibration Solutions (Thermo Fisher). Run order of samples was randomized and technical replicates were injected after every 4 samples to assess quality control. Raw files were searched against lipid databases using LipidSearch (Thermo Fisher).

### Metabolomic and lipidomic analysis

Metabolomics and lipidomics datasets were pre-processed using per-total normalization and feature standardization, on mean and standard deviation. Principal component analysis (PCA) was performed using prcomp (from stats v4.2.1 R package) function. Metabolic pathway level analysis of metabolomics data was performed by uploading separate lists of differentially abundant intracellular and extracellular metabolites to Metaboanalyst 5.0. Pathway Enrichment webtool. Pathway analysis parameters consisted of enrichment by Hypergeometric test and topology analysis by Relative-betweenness Centrality. All compounds in the *Homo sapiens* (SMPDB) pathway library were used as reference metabolome. Scatter plot was chosen as visualization method. Lipid moiety analysis for the intracellular lipidome was performed using the Substructure Analysis function of the LINEX$^2$ webtool.[42] Lipid pathway level analysis of the intracellular lipidomics data was performed using the Bioinformatics Methodology for Pathway Analysis (BioPAN) webtool.

### Proteomics analysis

Proteomics modalities were pre-processed using minimum value imputation of missing values, followed by median normalization.[88] Further analyses were performed using bulkAnalyseR v1.1.0[89] with differential expression calls using edgeR v3.40.2[90] and enrichment analysis performed on differentially expressed proteins using gprofiler2 v0.2.2.[91] The set of all genes expressed in matching RNAseq data was used as the background, only proteins expressed in >20% of cell lines were considered and FDR multiple testing correction was also performed.

### Multi-omics factor analysis (MOFA)

Multi-omics factor analysis (MOFA) was used to integrate intracellular lipidomics and secretomics modalities, using the MOFA2 v1.8.0 R package.[60] Replicates per cell line were pooled (by averaging); per-total normalization and feature scaling were also performed. Any proteins expressed in less than 20% of cell lines were removed from subsequent steps. MOFA imputation was performed for missing values in the secretomics data. A MOFA model was created using 3 factors (as recommended) and otherwise default settings. The calculate_variance_explained() and correlate_factors_with_covariates() functions from MOFA2 were used to assess the % variance explained by each factor, in each modality, and the correlation between each factor with disease and treatment covariates.

We noted a large number of missing values in the extracellular proteomic (secretomic) dataset, due to the detection limitations of the mass spectrometry-based method employed. In some cases, a consistent trend could be observed where only samples pertaining to a particular experimental group consistently produced a detectable signal, which was suggestive of a biologically relevant feature. In other cases, the signal across samples followed an inconsistent pattern, oscillating below and above the detection limit indiscriminate of a particular experimental group, which suggested technical variation. To prevent misattributing biological relevance to differences emerging from technical variation across samples we pre-filtered our dataset and removed any proteins expressed in less than 20% of cell lines from our analysis. The remaining missing values were imputed using the MOFA imputation approach; we acknowledge the impact the missing values and their imputation with limited information may have on conclusions.

### Multi-omics covariation network analysis

Multi-omics covariation network inference was performed using GENIE3 v1.20.0[92] across modalities and visualized using visNetwork v2.1.2; replicates were pooled per cell line (by averaging across replicates); all modalities were pre-processed using per-total normalization and feature scaling, with minimum value imputation for missing values and proteins expressed in <20% of cell lines removed in proteomics modalities. The top 1000 connections in the multi-omics networks were selected for visualization.

### SH-SY5Y in vitro cultures, neuronal differentiation

SH-SY5Y cells (gift from Michael Whitehead) were kept in culture and expanded in growth medium (DMEM/F12, 10% FBS, 1% Penicillin/Streptomycin). Growth medium was refreshed every 4 days. After reaching 80-90% confluency, SH-SY5Y cells were washed with warm 1X PBS, detached with Trypsin-EDTA 0.05%, and spun down at 300 x g for 5 min. Next, SH-SY5Y cells were counted and seeded at a density of 10.4 x $10^3$ cells/cm$^2$ in differentiation media (Neurobasal medium, 2% B27 supplement, 1% GlutaMAX, and 10 μM of all-trans retinoic acid [STEMCELL Technologies]). Differentiation media was replaced every other day until day 9 post-seeding, when SH-SY5Y neurons were exposed for 72h to conditioned NIM from the control or PMS iNSC lines.

### Generation of iNSC conditioned media for treatments

Control and PMS iNSCs were seeded in NIM with Y-27632 (10 μM) at a density of 100,000 cells/cm$^2$ onto GFR-matrigel coated 6 well plates. Medium was refreshed the next day with NIM supplemented with 10 μM of simvastatin or vehicle (ethanol) and cells were incubated for 48 hours. Medium was removed, cells were washed twice with 500 μL DPBS to remove simvastatin, and 1.5 mL of NIM was added to each well. After 24 hours conditioned medium (CM) was collected, spun at 300 x g for 5 minutes to remove debris and used immediately to treat SH-SY5Y neurons. For EphA4 blocking, conditioned media was incubated at 37°C with 1 μg/mL of the recombinant human EphA4 Fc chimera protein (R&D systems) or 1 μg/mL of the human IgG Fc control (R&D systems) for 30 minutes before exposure to differentiated SH-SY5Y cells. After 72 hours of CM exposure SH-SY5Y cells were collected for apoptosis and neuronal morphology assays.

### Apoptosis assay

To evaluate neuronal death SH-SY5Y cells were seeded and differentiated onto 13 mm diameter coverslips. Three coverslips were seeded per condition. After CM treatment cells were fixed with 4% paraformaldehyde, washed twice with PBS for 5 minutes, and blocked for 1 hour at room temperature in 0.1% PBST with 10% normal goat serum. Coverslips were then incubated at 4°C overnight with cleaved caspase 3 antibody (Cell Signaling,1:1000) in blocking buffer. Next the coverslips were washed three times with 0.1% PBST for 5 minutes, incubated with the appropriate secondary antibody (1:1000) in blocking buffer for 1 hour at room temperature, and then washed with PBS three times for 5 minutes. Lastly, the coverslips were counterstained with DAPI then mounted. 63x images pictures of 3 ROIs per coverslip were taken on a Leica DMI400B microscope. Images were batch analyzed using Fiji software; the pipeline included fluorescent signal identification by minimum error thresholding followed by the measurement of the mean gray value. The values from 3 ROIs were averaged out for each coverslip, and the resulting values were again averaged out to generate the mean fluorescence intensity (MFI) of each condition (e.g., neurons exposed to CM from PMS iNSC line A, neurons exposed to CM from control iNSC line B).

### Assessment of neurite length

SH-SY5Y cells were seeded and differentiated onto 6 well plates. Three wells were seeded per condition. After CM treatment SH-SY5Y neurons were imaged using an Echo Rebel microscope (Discover Echo) at 10x. Phase contrast images of 5 ROIs per biological replicate from each condition were taken. Images were converted to 8-bit and contrast was adjusted to make neurites easily visible using FIJI software. Data was quantified by a semi-automatically tracking NeuronJ plugin[93] from an average of >15 neurites per ROI. The values from 5 ROIs were averaged for each well, and the resulting values were averaged to generate the mean neurite lengths of each condition.

## QUANTIFICATION AND STATISTICAL ANALYSIS

ImageJ was used to analyze immunofluorescence and immunoblot images, and the detailed procedure is described in the ICC and immunoblot sections respectively. GraphPad Prism 10 for macOS was used to calculate statistics for non-omics data. Data was analyzed with the statistical test indicated in each figure. In the figure legends levels of significance (*$p<0.05$, **$p<0.01$, ***$p<0.001$, ****$p<0.0001$), along with statistical test and n are included.

Metabolomics and lipidomics datasets were pre-processed using per-total normalization and feature standardization, on mean and standard deviation. Principal component analysis (PCA) and PLS-DA analysis were performed using prcomp() (stats v4.2.1 R package) and plsda() [mixOmics v6.22.0 R package[94]] functions, respectively. Disease and treatment groups were compared using Wilcox rank sum with Benjamini-Hochberg multiple testing correction.

Proteomics datasets were pre-processed using minimum value imputation of missing values, followed by median normalization. Further exploratory analyses were performed using bulkAnalyseR v1.1.0[89] with differential expression calls using edgeR v3.40.2[90] with Benjamini-Hochberg multiple testing correction, and enrichment analysis performed on differentially expressed proteins using gprofiler2 v0.2.2.[91] The set of all genes expressed in matching RNAseq data was used as the background, only proteins expressed in more than 20% of cell lines were considered and FDR multiple testing correction was also performed.